

DEEP *Chandra* X-RAY IMAGING OF A NEARBY RADIO GALAXY 4C+29.30: X-RAY/RADIO CONNECTION

ANETA SIEMIGINOWSKA¹, ŁUKASZ STAWARZ^{2,3}, CHI C. CHEUNG⁴, THOMAS L. ALDCROFT¹, JILL BECHTOLD⁵, D. J. BURKE¹, DANIEL EVANS^{1,6}, JOANNA HOLT⁷, MAREK JAMROZY³, GIULIA MIGLIORI¹

¹ Harvard Smithsonian Center for Astrophysics, 60 Garden St, Cambridge, MA 02138, USA

² Institute of Space and Astronautical Science, JAXA, 3-1-1 Yoshinodai, Sagami-hara, Kanagawa, 229-8510, Japan

³ Astronomical Observatory, Jagiellonian University, ul. Orla 171, 30-244 Kraków, Poland

⁴ National Research Council Research Associate, National Academy of Sciences, Washington, DC 20001, resident at Naval Research Laboratory, Washington, DC 20375, USA

⁵ Steward Observatory, University of Arizona, 933 North Cherry Avenue, Tucson, AZ 85721, USA

⁶ Elon University, Department of Physics, 100 Campus Drive, Elon, NC 27244, USA

⁷ Leiden Observatory, Leiden University, PO Box 9513, 2300 RA Leiden, The Netherlands

asiemiginowska@cfa.harvard.edu

Draft version February 25, 2013

ABSTRACT

We report results from our deep *Chandra* X-ray observations of a nearby radio galaxy, 4C+29.30 ($z = 0.0647$). The *Chandra* image resolves structures on sub-arcsec to arcsec scales, revealing complex X-ray morphology and detecting the main radio features: the nucleus, a jet, hotspots, and lobes. The nucleus is absorbed ($N_{\text{H}} \simeq 3.95^{+0.27}_{-0.33} \times 10^{23} \text{ cm}^{-2}$) with an unabsorbed luminosity of $L_{2-10 \text{ keV}} \simeq (5.08 \pm 0.52) \times 10^{43} \text{ erg s}^{-1}$ characteristic of Type 2 AGN. Regions of soft ($< 2 \text{ keV}$) X-ray emission that trace the hot interstellar medium (ISM) are correlated with radio structures along the main radio axis indicating a strong relation between the two. The X-ray emission beyond the radio source correlates with the morphology of optical line-emitting regions. We measured the ISM temperature in several regions across the galaxy to be $kT \simeq 0.5 \text{ keV}$, with slightly higher temperatures (of a few keV) in the center and in the vicinity of the radio hotspots. Assuming these regions were heated by weak shocks driven by the expanding radio source, we estimated the corresponding Mach number of 1.6 in the southern regions. The thermal pressure of the X-ray emitting gas in the outermost regions suggest the hot ISM is slightly under-pressured with respect to the cold optical-line emitting gas and radio-emitting plasma, which both seem to be in a rough pressure equilibrium. We conclude that 4C+29.30 displays a complex view of interactions between the jet-driven radio outflow and host galaxy environment, signaling feedback processes closely associated with the central active nucleus.

Subject headings: radiation mechanisms: non-thermal — galaxies: active — galaxies: jets — galaxies: individual (4C+29.30) — X-rays: galaxies

1. INTRODUCTION

Recent observational and numerical studies highlight the importance of active galactic nuclei (AGN) induced feedback on the co-evolution of a super-massive black hole (SMBH) and its host galaxy (Silk & Rees 1998; Merloni & Heinz 2008). Various physical processes involved are in many respects only poorly understood, although the emerging agreement is that this feedback must have played a significant role during the primary epochs of galaxy formation at high redshifts (Croton et al. 2006).

The impact of a SMBH on the larger scale environment has been evidenced by powerful AGN outflows (see e.g., Tadhunter 2007). In particular, it has been established that substantial amounts of energy have been deposited to the intergalactic medium by powerful radio-emitting outflows associated with massive elliptical galaxies located in galaxy clusters (e.g., Nulsen et al. 2005), and that relatively dense optical line-emitting gas participates in galaxy scale outflows (e.g., Morganti et al. 2005; Holt et al. 2008). The highest angular resolution X-ray observations performed by the *Chandra* X-ray Observatory (*Chandra*) proved to be particularly important in

studying the physics of the jet-related feedback, since they provided direct evidence for the interactions between the radio-emitting outflows and surrounding gas, most prominently in the case of clusters of galaxies (McNamara & Nulsen 2007), but also in central regions of nearby galaxies (Hardcastle et al. 2007; Wang et al. 2011a,b). However, only in a few cases could the details of such interactions be accessed, with a complex picture involving recurrent AGN outbursts shaping the properties of the interstellar and intergalactic medium at different evolutionary stages of the systems being revealed.

Among a few sources where the jet-ambient medium interactions (particularly within the confines of the host galaxies) can be traced with sufficient details at X-ray frequencies are the well-known radio galaxies M 87 and NGC 1275 (e.g., Million et al. 2010; Fabian et al. 2011, respectively) and the brightest nearby Seyfert galaxy NGC 4151 (Wang et al. 2010). The nearest radio-loud AGN, Centaurus A (distance $D \simeq 3.7 \text{ Mpc}$) is a well-known example where the rejuvenated radio structure and jet-ambient medium interactions can easily be mapped at various scales and different frequencies (e.g., Morganti

2010, and references therein). In all these cases, the X-ray observations exposed signatures of shocks or shock heated medium, ionization of the gas, the scales of the impact of the radio source on the medium and most importantly, the overall energetics of the systems. Such investigations of the feedback processes at various stages of the AGN activity are highly desirable, however, they can only be performed for nearby galaxies given the capabilities of the currently operating X-ray missions.

To investigate such feedback processes, we selected the low-redshift radio galaxy 4C+29.30 (0836+299, $z = 0.0647$, $D \simeq 287$ Mpc)¹ for an in-depth X-ray study with *Chandra*. At optical frequencies, the moderate-luminosity of its nucleus resembles that of Seyfert type 2 galaxies. The radio source displays a transitional FRI/FRII radio morphology and intermediate radio luminosity of the order of $\sim 10^{42}$ erg s⁻¹. It is hosted by an elliptical galaxy characterized by a distorted structure due to a relatively fresh merger with a gas-rich companion (van Breugel et al. 1986). The radio structure extends out to ~ 30 kpc from the center of the galaxy and consists of a prominent one-sided jet and lobe visible to the south, and a counter-lobe to the north. No counterjet has been detected at radio frequencies indicating an intermediate jet inclination to the line of sight and relativistic beaming involved. 4C+29.30 is particularly interesting due to its prominent ($\sim 10^{43}$ erg s⁻¹) and extended (~ 30 kpc) emission-line regions intertwined with the described radio structure on scales that can be resolved with *Chandra* ($1'' = 1.227$ kpc at the redshift of the source). As argued in van Breugel et al. (1986), this complex morphology and the overall energetics of the line-emitting gas suggest strong interactions between the radio outflow and the cold clumpy phase of the gaseous environment in this system, which is therefore specially well-suited for the observational investigation of the feedback process.

Similarly to the case of Centaurus A, the inner radio structure and the host galaxy of 4C+29.30 are surrounded by a ~ 600 kpc diffuse radio emission which extends in the N-S direction (Jamrozy et al. 2007). The primary (inner/young) and outer radio structures are relatively well-aligned, as observed in the class of so-called ‘double-double’ radio galaxies (see Saikia & Jamrozy 2009, for a review of sources of recurrent jet activity in general). The presence of these outer lobes indicate a highly intermittent jet activity in the source with the young (~ 33 Myr) kpc-scale outflow propagating within relic lobes formed in a previous epoch of the jet activity (some $\gtrsim 200$ Myrs ago). We note that modulated jet activity resulting in the formation of multiple radio lobes was also claimed in the cases of the radio galaxies M 87 and NGC 1275 located in rich clusters (e.g., Owen et al. 2000; Fabian et al. 2000), albeit on scales much smaller than that of the outer radio halos in 4C+29.30 and Centaurus A.

In the X-rays, 4C+29.30 was not detected by ROSAT (Canosa et al. 1999) and the first such detection of the source was obtained by *Chandra*. This initial *Chandra* observation from April 2001 (ObsID=2135) was short (~ 8 ksec), but provided a snap-shot view of the source’s complex X-ray morphology, including the X-ray detection of the nucleus and radio hotspots, and possible indication

of an X-ray jet and diffuse components as well (Gambill et al. 2003; Sambruna et al. 2004; Jamrozy et al. 2007). However, this early observation did not provide constraints on the energetics of the system or the nature of the X-ray emission in different regions due to the very limited photon statistics.

To address the above issues and to discuss in more detail the jet-related feedback in 4C+29.30, we obtained new deep high angular resolution X-ray observations of the source with *Chandra*. The new *Chandra* data provide the high quality X-ray imaging of a radio source with an extended optical emission-line region revealing their complex relationship. The results of our study are presented here. In the following, we begin by discussing the technical settings of the observation and analysis methods in Section 2. We then show details of the X-ray morphology in Section 3 and the results of spectral analysis of individual X-ray features in Section 4. We finally discuss and summarize the main results in Sections 5 and 6, respectively.

2. CHANDRA OBSERVATIONS AND ANALYSIS METHODS

Deep *Chandra* ACIS imaging observations of 4C+29.30 were performed in February 2010. The approved 300 ksec observation was split into four separate pointings that sum to a total exposure of 286.4 ksec (see Table 1 for details). The source was placed on the back-illuminated CCD (S3) and was offset by -1 arcmin in Y coordinates to ensure that the diffuse galaxy emission was positioned away from a chip gap. The observations were made in VFaint mode and the full-window mode. The background was quiet and the observations were not affected by Solar flares. The four pointings were performed with similar enough configurations that they could be merged together for the purpose of image analysis. Note that the exposure maps are flat on the scale size of the galaxy in all four observations. Analysis was performed with the CIAO version 4.3 software (Fruscione et al. 2006) using CALDB version 4.4. All spectral modeling was done in Sherpa (Freeman et al. 2001; Refsdal et al. 2009). We used the Cash and Cstat fitting statistics (Cash 1979) and the Nelder-Mead optimization method (Nelder & Mead 1965).

We processed the data by running CIAO tool `acis-process-events` and applied the newest calibration files, filtered VFaint background events, and ran a sub-pixel event-repositioning algorithm (and set `pix_adj=EDSER`). This final step provides the highest angular resolution X-ray image data for the most up-to-date ACIS-S calibration. While the four separate observations were merged into one in order to obtain the best quality image for studying the X-ray morphology, for all spectral modeling, we extracted the spectra and response files from the individual observations.

3. X-RAY MORPHOLOGY

Figure 1 shows our new *Chandra* ACIS-S X-ray image of the galaxy 4C+29.30 obtained from the summed 286.4 ksec exposure. The image is overlaid with the radio contours from VLA 1.45 GHz map of van Breugel et al. (1986). A complex morphology with many regions of enhanced emission is displayed in this image. The X-ray emission spans

¹ We assume the following cosmological parameters: $H_0 = 71$ km s⁻¹ Mpc⁻¹, $\Omega_M = 0.27$, $\Omega_{vac} = 0.73$.

about ~ 60 kpc in total extent and is marked by a pronounced center and two bright components coincident with the jet termination regions (the radio ‘hotspots’). The low surface brightness diffuse X-ray emission connecting the hotspots along the jet axis, together with the previously unknown linear X-ray feature almost perpendicular to the radio axis (in the NE-SW direction), creates an overall impression of an X-like shape for the diffuse X-rays. We identify and mark these various X-ray emission regions in Figure 2.

Figure 3 presents the smoothed X-ray images in the soft ($0.5 - 2$ keV) and hard ($2 - 7$ keV) bands. As seen in the images, most of the diffuse structure is suppressed above ~ 2 keV. The dominant core (hereafter denoted as ‘Core’) and the Southern hotspot (‘SHspot’) are in fact the only features detected at photon energies > 2 keV (note however the dramatically decreased prominence of SHspot in the hard band). In contrast, the soft band image shows a complex and rich morphology with several distinct features, either relatively compact blobs or extended filaments, and the quite prominent horizontal branch perpendicular to the main axis of the radio source.

Figure 4 shows the soft and hard X-ray images of the central region of the galaxy (‘Center’). The soft emission is diffuse within the inner $8''$. The hard emission is concentrated within a circular region with $1.5''$ radius centered on the nucleus, with no sign of any extended emission component, thus is most likely dominated by the central AGN.

In Figure 5 we show radio contours from a VLA 5 GHz image overlaid on the smoothed $0.5 - 2$ keV ACIS-S image. The linear X-ray emission component extending from the core to the south (hereafter ‘SJet’) is closely aligned with the radio jet. Note that the SJet feature covers a much broader area than the well-defined radio jet, and hence it is not obvious if all the X-rays are non-thermal in origin. The radio jet terminates at a hotspot $\sim 20''$ away from the core, where the whole (radio) outflow suddenly decollimates and extends further to the south in a much less organized fan-like pattern (see also Figure 1). The X-ray emission aligned with the radio jet flares similarly at the position of SHspot, but it is not clear if the X-rays follow the radio morphology also further to the South (‘SLobe1’ region).

The X-ray emission component detected to the north of the core extends over a $30''$ wide band roughly perpendicular to the main radio source axis. This emission has a rather complex morphology and coincides roughly with the position of an extended optical emission-line region analyzed in detail by van Breugel et al. (1986). Here, we can identify the X-ray counterpart of the northern radio hotspot (hereafter ‘NHspot’), as well as its extension to the west forming a lower-surface brightness tail (‘NLobe’). This tail may however simply be a superposition of some smaller-scale enhancements visible in the field rather than a truly coherent feature. Indeed, a zoomed-in view of the northern region presented in Figure 6 shows that the X-ray emission beyond the NHspot radio extent forms an apparent wiggly filamentary feature approximately perpendicular to the radio axis.

In general, it appears that the X-ray emission in the

northern region coincides better with the line-emitting gas than with the radio-emitting plasma, and that the X-ray emission even “hugs” the northern radio lobe on its eastern side from the outside (‘EArm’ component in Figure 2). It is therefore possible that the bulk of the X-ray emission here could be associated with the thermal gas that is being shocked by the expanding radio source, rather than with the non-thermal emission of relativistic plasma injected by the radio jet into the expanding lobes. This idea is strongly supported by the fact that the brightest northern X-ray features (with the exception of NHspot) are located near the boundaries of the radio structures, and also by the spectral analysis presented below (Section 4).

We identified two X-ray features ‘HBranchS’ and ‘HBranch’ located almost perpendicular to the radio source axis. There is no obvious correspondence between these features and the line-emitting gas. A faint optical filament of a similar (projected) size as the radio jet, but misaligned (by about $\sim 20^\circ$) with the jet axis (van Breugel et al. 1986) is oriented in between the jet and the ‘HBranchS’. However, prominent dust lanes seen in the optical HST image are located in the similar direction to these X-ray features suggesting a possible relation between the two. The optical studies support an idea of a merger event in which a smaller rich galaxy was captured and the dust shells are the remnants from that event. Thus the observed X-ray morphology appears to be shaped by a complex mixture of a merger and a radio source activity, and both influencing the properties of the ISM.

4. X-RAY SPECTRAL PROPERTIES

We extracted X-ray spectra and created calibration response files for each of the four individual *Chandra* observations using the specified regions marked on Figure 2 and listed in Table 2. The response files are based on CALDB 4.4 and include the updated ACIS-S contamination model². The spectra from the four observations were fitted simultaneously in Sherpa using Cash statistics with the `simplex-neldermead` and `moncar` methods. The background and source spectra were fit simultaneously assuming several different parametrized models (see below). We used the blank-sky background data to create a background model that was then scaled to our observations (for details, see Siemiginowska et al. 2010). For the features embedded in the diffuse emission, we also included background model components that accounted for the diffuse emission contributing to the source spectrum. The modeling details for all the features are described below.

We modeled the spectra of all the features defined in Section 3 assuming two main emission models: an absorbed power-law model and an absorbed thermal emission model. In the latter case we used the APEC³ thermal model describing emission from collisionally ionized plasma, which allows for varying metal abundances. For most of the regions fitted with this model we found low values of the abundance parameter, and for the regions located further away from the galaxy center we could only determine the upper limits ($< 10\%$ solar). Similar abundance profiles are often found in elliptical galaxies. On the other hand there are many systematic issues related to fit-

² <http://cxc.harvard.edu/ciao/why/acisqecontam.html>

³ Model of the emission from collisionally ionized plasma based on ATOMDB, <http://www.atomdb.org/>

ting the abundances in multi-phase ISM using low signal to noise data (see Kim 2012, for details). For this reason we favor the best fit model parameters emerging from the thermal fits consisting of a pure thermal bremsstrahlung emission, obtained by setting the abundance parameter in the APEC model to 0. This choice reduces the number of free model parameters critical in modeling limited photon statistics data. However, for completeness, we provide the best fit APEC model parameter values obtained with the abundance parameter set free to vary. The best-fit parameters for all the regions, including the resulting unabsorbed X-ray fluxes in the soft (0.5 – 2 keV) and hard (2 – 10 keV) bands, for both models are summarized in Tables 4 and 5, respectively. The model results for the nucleus, which required a more sophisticated treatment, are given separately in Table 3. The quoted errors are 1σ for one significant parameters, unless specifically noted.

4.1. The Nucleus

Based on the soft and hard X-ray band images of the source, it is apparent that the unresolved nucleus, unlike the diffuse structure surrounding it, is bright at photon energies exceeding about 2 keV. Utilizing the hard band image (2 – 7 keV; see Figure 3), we measured a centroid for the nucleus at $\alpha(\text{J2000})=08^h40^m02^s.3$, $\delta(\text{J2000})=+29^\circ49'02''.57$. This position agrees with that of the galaxy centroid quoted in NED based on the Sloan Digital Sky Survey DR6⁴.

We defined the nucleus (core) region as a circle with a radius equal to $1.25''$ centered on the above position and extracted the X-ray spectra and response files for that region. A total of 5328 ± 73 counts (5303.7 ± 73.2 net counts) with photon energies between 0.5 keV and 7.0 keV were found. Approximately $\sim 90\%$ of the detected counts have energies between 2 keV and 7 keV. We note that the expected pileup fraction for the counts in the nucleus is low, $< 2\%$, and we neglected the pileup effects in our analysis. To account for the local background contribution to the core emission, we assumed an annulus region centered on the core position with an inner radius of $1.5''$ and an outer radius of $10''$. In fitting the background spectrum, we assumed a model composed of a thermal bremsstrahlung emission and power-law component, and the resultant fitted parameters are summarized in Table 3.

The *Chandra* spectrum of the core was poorly fitted with an absorbed power law model, with $\chi^2_\nu = 2.56$ in the standard χ^2 test applied to the binned data and $\nu=453$ degrees of freedom. Therefore, we attempted to fit the core spectrum with several parametric models that consisted of absorbed and unabsorbed emission components. All models included the Galactic absorption column density of $N_{\text{H}}(\text{Gal}) = 3.98 \times 10^{20} \text{ cm}^{-2}$ (Dickey & Lockman 1990). Our selection of models and their best-fit parameters are listed in Table 3. We found that the nucleus is significantly absorbed with a relatively high intrinsic absorption column density of $N_{\text{H}}(\text{int}) = 3.95^{+0.27}_{-0.33} \times 10^{23} \text{ cm}^{-2}$ and that the unabsorbed lower energy X-ray spectrum constitutes a separate emission component. This type of a composite spectrum consisting of an unabsorbed soft X-ray emission and a highly absorbed hard X-ray component is often found in the centers of radio galaxies (Hardcastle et

al. 2009).

To fit the hard band X-ray emission detected from the core, we assumed an absorbed power-law model. In this model, the best-fit photon index was $\Gamma = 1.70^{+0.38}_{-0.36}$ ($N_{\text{H}}(\text{int})$ as given above) and the resultant unabsorbed flux of $(5.1 \pm 0.5) \times 10^{-12} \text{ erg cm}^{-2} \text{ s}^{-1}$ corresponds to a 2 – 10 keV luminosity of $(5.0 \pm 0.5) \times 10^{43} \text{ erg s}^{-1}$. We note that the derived values of the photon index and luminosity of the nucleus in 4C+29.30 are similar to the ones found in the nuclei of Seyfert galaxies (Singh et al. 2011). In Section 5 we discuss implications of the luminous nucleus on the physical state of the environment in this object.

The observed soft (0.5-2 keV) unabsorbed emission component contains only about $\sim 10\%$ of the total counts detected from the core. We first tried to model this emission with an unabsorbed power-law component which was added to the absorbed power-law model discussed earlier, fitting both components simultaneously. We obtained a reasonable photon index of $\Gamma_s = 1.60 \pm 0.12$ and a 0.5 – 2 keV flux of $6.4 \times 10^{-15} \text{ erg cm}^{-2} \text{ s}^{-1}$ for this model. Next, instead of a power law model, we tried two types of thermal models added to the intrinsically absorbed power-law component: a bremsstrahlung emission and the APEC plasma model. Both thermal models gave a good description of the soft emission. The best-fit temperature of the bremsstrahlung emission is equal to $kT_b = 6.8^{+9.9}_{-2.5} \text{ keV}$, while the APEC gave a slightly higher, but consistent (within the errors) temperature of $kT_a = 9.6^{+10.0}_{-4.8} \text{ keV}$ and 3σ upper limit to the metal abundances of $A < 1.35$ with respect to the Solar value. For the bremsstrahlung model, we measure a 0.5 – 2 keV flux of $7.1 \times 10^{-15} \text{ erg cm}^{-2} \text{ s}^{-1}$ corresponding to a luminosity of $6.9 \times 10^{40} \text{ erg s}^{-1}$. Although we were unable to discriminate statistically between any of the above models for the soft component, we discuss a possible origin of this soft emission in Section 5.

4.2. X-ray Jet

We selected a narrow box region (marked in Figure 2 as SJet) to delineate the X-ray emission to the south of the nucleus to study the emission that could be associated with the known radio jet at that location. We fitted both an absorbed power-law and an absorbed thermal model to the X-ray spectrum of this region (see Tables 4 and 5, respectively). In the power-law model, we obtained a photon index, $\Gamma = 2.2 \pm 0.2$, when we fixed the absorption parameter at the Galactic value, and obtained only upper limits to both the absorbing column and photon index when the absorption parameter was left free in the fit. The upper limit to the absorption is consistent with the Galactic column thus we conclude that there is no intrinsic absorption of the X-ray emission from this jet region. In the framework of the thermal model, we obtained the best fit temperature of $kT_b = 2.1^{+0.9}_{-0.6} \text{ keV}$ (68% uncertainties for 1 significant parameter). We could only obtain a 3σ upper limit of $A < 0.13$ of the Solar values for the metal abundances in this region.

The total luminosity in the jet assuming the best-fit power-law model is equal to $1.4 \times 10^{40} \text{ erg s}^{-1}$ in the 0.5 – 2 keV range, which is comparable to the luminosity in the hard band (2 – 10 keV) of $1.2 \times 10^{40} \text{ erg s}^{-1}$. The thermal versus non-thermal origin for the X-ray emission

⁴ <http://www.sdss.org/dr6/>

detected from SJet is discussed in Section 5.

4.3. Hotspots

There are two enhanced regions of X-ray emission in the *Chandra* image located near the opposite extremes of the radio source. They appear to be associated with the radio hotspots, although the northern radio feature does not display a prominent hotspot in the VLA map. The X-ray images shown in Figure 3 indicate that the northern hotspot emission is rather soft, as it is very faint in the hard band image. In contrast, the hotspot to the south is quite prominent in the the hard band image. We extracted the spectra of both features assuming circular regions with $1.2''$ radius each and fit the data assuming a single absorbed power-law model and a thermal emission model. In both cases, we both fixed the absorption column at the Galactic value and set it free in the fits.

4.3.1. Southern Hotspot - the end of a Jet

The best-fit model parameters for the southern hotspot are listed in Tables 4 and 5. The best-fit power-law photon index for the model with Galactic absorption only ($\Gamma = 2.16 \pm 0.08$) is consistent with the previous determination based on the analysis of the original shorter 8ksec *Chandra* data (Sambruna et al. 2004; Jamrozy et al. 2007), but now with improved photon statistics. When the absorption was allowed to vary in the fit, we obtained a value of the intrinsic column density, $N_H = (6.0 \pm 4.0) \times 10^{20} \text{ cm}^{-2}$, consistent with the Galactic column, and a photon index ($\Gamma = 2.24_{-0.16}^{+0.15}$) similar to the above value. The resulting model fluxes in the soft and the hard bands are equal to $F_{0.5-2\text{keV}} = 7.75 \times 10^{-15} \text{ erg cm}^{-2} \text{ s}^{-1}$ and $F_{2-10\text{keV}} = 6.27 \times 10^{-15} \text{ erg cm}^{-2} \text{ s}^{-1}$, corresponding to luminosities of $7.7 \times 10^{40} \text{ erg s}^{-1}$ and $6.2 \times 10^{40} \text{ erg s}^{-1}$, respectively. Besides the nucleus, the southern hotspot is the only feature with significant emission above 2 keV, thus signaling non-thermal processes at work, as in fact expected at the termination region of a relativistic jet, or a presence of a particularly hot X-ray emitting gas in the immediate hotspot vicinity. Indeed, for the thermal model fit, the fitted temperature appears relatively high with $kT_a = 2.3_{-0.2}^{+0.3} \text{ keV}$ and a 3σ upper limit for the metal abundances of < 0.09 with respect to Solar.

Next, we modeled the X-ray emission immediately outside the southern hotspot (region SLobe1), as well as within the more extended diffuse emission to the south-east (SLobe; see Tables 4 and 5). For the power-law model, the fitted X-ray spectrum of SLobe1 is characterized by a photon index of $\Gamma = 2.09_{-0.26}^{+0.28}$, which is very similar to that of SHspot. The best-fit thermal model for this emission component shows a relatively high temperature of $kT_b = 2.24_{-0.74}^{+1.40} \text{ keV}$. We cannot discriminate between a thermal and non-thermal origin of this emission statistically because of the low signal-to-noise data. However, from the physical point of view, the emission of SLobe1 corresponding to the soft and hard luminosities roughly $10^{40} \text{ erg s}^{-1}$, could well be a mixture of both thermal and non-thermal photons (see Section 5 below).

On the other hand, the best fit model parameters for SLobe are quite different than for the SLobe1 region discussed above. The best-fit photon index of the power-law model fit to the SLobe spectrum, $\Gamma = 2.73_{-0.23}^{+0.24}$, is larger

than the one evaluated for SLobe1. Not surprisingly, in the case of the thermal model, the best-fit temperature for the SLobe spectrum is significantly lower than the one obtained for SLobe1, namely $kT_b = 0.8 \pm 0.2 \text{ keV}$. These results may indicate that in the observed X-ray emission in the SLobe feature is purely thermal in origin. Yet, the derived gas temperature is slightly higher than that of the analogous structure to the North (discussed below).

4.3.2. Northern Hotspot

The best-fit photon index in the power-law model for the X-ray feature NHspot was determined as $\Gamma = 3.34_{-0.15}^{+0.16}$, assuming Galactic absorption only. Its spectrum is therefore much steeper than that determined for SHspot. The spectrum appeared even steeper ($\Gamma = 5.0_{-0.1}^{+0.1}$) when the absorption column was allowed to vary during the fit, returning $N_H = 3.32_{-1.00}^{+1.12} \times 10^{21} \text{ cm}^{-2}$ well in excess of the Galactic value, but significantly less than the column measured for the nucleus. These results may imply either a non-negligible intrinsic absorption of the non-thermal X-ray continuum of NHspot, possibly related to the presence of line-emitting gas in the vicinity of the hotspot, or a thermal origin of the X-ray emission of the hotspot. In the framework of the thermal scenario we obtained a modest temperature of the emitting plasma $kT_b = 0.54_{-0.04}^{+0.06} \text{ keV}$ and $0.49_{-0.06}^{+0.07} \text{ keV}$ for both frozen and free absorption column, respectively. (We note that in the latter case, the intrinsic absorption $N_H = 7.8_{-5.8}^{+6.7} \times 10^{20} \text{ cm}^{-2}$ turned out anyway to be consistent with the Galactic value.) The soft (0.5 – 2 keV) and hard (2 – 10 keV) luminosities of NHspot (corrected for absorption) are $4.5 \times 10^{40} \text{ erg s}^{-1}$ and $1.5 \times 10^{39} \text{ erg s}^{-1}$, respectively. Even though spectrum has only 242.7 ± 15.8 net counts in 0.5 – 7 keV band we were able to fit the abundances (for the absorption fixed at the Galactic value) and obtained the best fit value of $A = 0.06_{-0.02}^{+0.03}$ with a slightly higher value of the temperature, $kT_a = 0.79_{-0.06}^{+0.06} \text{ keV}$. We note that in this model these two parameters, N_H and A , are correlated and the true uncertainties on both parameters are larger. In addition our very low counts spectrum would not resolve any multi-temperature structures resulting in the artificially low abundances.

NHspot is the brightest X-ray feature in the northern region being embedded within the defined larger-scale NLoBe region where the soft X-ray emission is rather diffuse. We modeled the NLoBe spectrum with a thermal model and obtained $kT_b = 0.45_{-0.08}^{+0.05} \text{ keV}$ when we apply Galactic absorption only and a slightly lower temperature $kT_b = 0.33_{-0.08}^{+0.09} \text{ keV}$ with a relatively strong absorption of $N_H = 1.57_{-0.08}^{+0.91} \times 10^{21} \text{ cm}^{-2}$. The NLoBe temperature is in good agreement with the temperature estimated above for the NHspot which strongly supports a thermal origin of the X-ray emission from the hotspot. We note that the abundances are low $0.06_{-0.02}^{+0.03}$ and consistent with the value found for NHspot above. The 0.5 – 2 keV unabsorbed luminosity of the entire NLoBe region assuming the thermal model is equal to $7.5 \times 10^{40} \text{ erg s}^{-1}$, which is about twice the luminosity of NHspot in the same band.

We also modeled the spectra of the region which corresponds to the outermost northern enhancements visible on the edges of the radio lobe, NLoBe1 (see Figure 6). We obtained a significantly higher temperature

($kT_b = 1.9^{+1.0}_{-0.5}$ keV) for NLOBE1 than for the other parts of the northern X-ray emission. It is also interesting to note that a power-law model fit to the X-ray spectra of NLOBE1 gave $\Gamma = 2.16 \pm 0.28$, which agrees with the photon indices of SHspot and also SJET. Thus this emission may be of a different origin than the emission from NLOBE and NHspot and be more closely related to the radio outflow and interaction with the ambient medium. We continue our discussion of the northern emission in Section 5 below.

4.4. Diffuse Emission

We identified several distinct X-ray emission regions across the galaxy in addition to the main morphological features shown above. They are indicated in Figure 2 as EArm, HBranch, and HBranchS. These regions were modeled with both an absorbed power-law model and a thermal emission (see Tables 4 and 5, respectively). The best-fit model parameters for the EArm and HBranch regions are identical, with $\Gamma = 3.53$ for the power-law and $kT_b = 0.39$ keV for a thermal model fit. The metal abundances are similar for both regions with $A = 0.13 - 0.18$ of the Solar value for the temperature of $kT_a = 0.7$ keV. The HBranchS spectrum has a slightly higher best-fit temperature of $kT_b = 0.52^{+0.06}_{-0.05}$ keV and lower but consistent metal abundance of $0.09^{+0.08}_{-0.04}$ for $kT_a = 0.75$ keV. The total $0.5 - 2$ keV luminosities (corrected for absorption) of all three components are relatively high and equal to 9.1×10^{41} erg s $^{-1}$. The total contribution of these diffuse components to the total emission in the hard X-ray band is at least 3 orders of magnitude lower. The thermal origin of these regions is advocated in Section 5 below.

5. DISCUSSION

We have presented new, deep *Chandra* X-ray observations of the radio source, 4C+29.30, hosted by a nearby ($z = 0.0647$) post-merger elliptical galaxy. The double-double radio morphology of this system consists of Mpc-size relic lobes and a smaller-scale, younger radio source (Jamroz et al. 2007, Section 1). Our X-ray observations focused on the smaller-scale (inner tens of kpc-size) radio structures where we could study the effects of interactions between the expanding radio source and the ISM.

4C+29.30 could be viewed as an analogue to the famous radio galaxy Centaurus A (Israel 1998). They display a similar morphology with a pronounced dust lane and cold gas situated across the galaxy perpendicular to the radio source axis, but the former is slightly more powerful at radio frequencies than Centaurus A. 4C+29.30 is also characterized by a luminous extended emission-line region which is of the same size ($\sim 50 - 60$ kpc) as the inner radio source. van Breugel et al. (1986) studied a connection between the radio source and line-emitting gas using VLA and ground-based optical data. They suggested that the gas is most likely dragged from the inner parts of the host galaxy, accelerated, and partly entrained by the radio-emitting plasma outflowing from the nucleus. The process responsible for the ionization of the line-emitting gas far away from the nucleus remained vague however.

Our *Chandra* X-ray observations of 4C+29.30 add a new dimension to studies of the physics of radio source interactions with the ISM in general. The new deep X-ray dataset

enabled us to determine the overall energetics of the system with much improved detail over the earlier studies in the radio and optical bands. The *Chandra* image revealed a remarkable X-ray morphology on the scale of the young radio source and the extended emission-line region, with complex diffuse filaments and compact blobs partly overlapping with the radio-emitting plasma, and partly with the line-emitting gas. The spectral analysis carried out for several of the brightest X-ray features indicated a mixture of thermal and non-thermal emission components, characterized by a variety of temperatures and spectral slopes. We also detect possible variations in metal abundances of the hot ISM with the high abundances in the center and the very low values (< 0.1 of the Solar) in the outer regions of the galaxy. However, the quantitative measurements of the abundance variations are not possible with the current data. The presented results support and strengthen the conclusions regarding the feedback process operating in 4C+29.30, which we discuss below.

5.1. Nucleus of 4C+29.30

Even though the nucleus of 4C+29.30 was detected in X-rays already in the previous short *Chandra* observation (Gambill et al. 2003), only now can we study its properties in details using the new high-quality spectrum at keV photon energies. The new observations confirmed that the AGN is buried within a large amount of gas and the AGN emission is only visible at the high energy X-rays where the effect of the strong absorption is less substantial. The measured intrinsic absorption column of $N_H = 3.95^{+0.27}_{-0.33} \times 10^{23}$ cm $^{-2}$ is consistent with the values reported earlier by Gambill et al. (2003) and Jamroz et al. (2007). This X-ray absorption is due to both the neutral and ionized gas. The neutral Hydrogen column density of the in-falling gas based on the redshifted HI absorption lines reported by Chandola et al. (2010) is equal to $N_{HI} \simeq 5 \times 10^{21}$ ($T_s/100$ K) cm $^{-2}$, where T_s is the spin temperature. The standard assumption of $T_s \sim 100$ K results in almost two orders of magnitude smaller neutral column than the total one measured in X-rays, i.e., $N_{HI} \ll N_H$. Only with much larger spin temperatures (which might in fact be expected in the AGN environment) could the neutral Hydrogen column density around the nucleus of 4C+29.30 be comparable to the total equivalent Hydrogen column density inferred from our X-ray observations (see in this context the discussion in Ostorero et al. 2010). Note that large amounts of in-falling matter inferred from the redshifted HI absorption lines are usually observed in rejuvenated and newly born radio sources (e.g., Gupta et al. 2006; Saikia et al. 2007, and references therein), including also the case of Centaurus A (Morganti et al. 2008).

The nuclear X-ray luminosity of 4C+29.30 is equal to $L_{2-10 \text{ keV}} \simeq 5 \times 10^{43}$ erg s $^{-1}$, a value typical of nearby Seyfert-type AGNs (Singh et al. 2011). This, together with the best-fit photon index for the hard X-ray nuclear continuum ($\Gamma \simeq 1.7$; representative of Seyferts and radio galaxies), suggests that the observed radiation is related to the standard AGN engine, i.e., X-ray emission from a hot corona reprocessing thermal optical/UV radiation from an accretion disk (see e.g., Chiang 2002; Sobolewska et al. 2004a,b). In the case of 4C+29.30, the exact level of the accretion-related UV luminosity is un-

clear because of the significant absorption affecting the observed central optical/UV radiation. However, assuming a typical value of the UV-to-X-ray luminosity ratio found in AGN samples corresponding to a power-law slope of $\alpha_{\text{ox}} \equiv -0.3838 \times \log[L_{2\text{keV}}/L_{2500\text{\AA}}] \simeq 1.5$ (Kelly et al. 2007; Sobolewska et al. 2009), one can evaluate the optical/UV luminosity of the 4C+29.30 nucleus to be roughly $\sim 10^{45} \text{ erg s}^{-1}$. On the other hand, if we assume a bolometric correction factor of 70 for Seyfert 2 galaxies, as advocated by Singh et al. (2011), we obtain a bolometric luminosity of $3.5 \times 10^{45} \text{ erg s}^{-1}$.

We note that 4C+29.30 has recently been detected at photon energies exceeding 10 keV and up to $\sim 150 \text{ keV}$ by the *Swift*/BAT (Baumgartner et al. 2010). The photon index of a power-law model reported in the *Swift*/BAT 58-month catalog⁵ of $\Gamma_{\text{BAT}} = 1.65^{+0.45}_{-0.42}$ agrees with the photon index we found in our *Chandra* spectra of the nucleus. We note that the reported *Swift*/BAT luminosity in 14 – 150 keV energy range is equal to $1.7 \times 10^{44} \text{ erg s}^{-1}$. This emission is most likely related to the disk corona in the Seyfert-type core of 4C+29.30. This provides additional evidence for the intrinsic high luminosity of the AGN buried in the 4C+29.30 center as we concluded based on the new *Chandra* data.

Our estimated AGN luminosity is comparable to the accretion-related luminosities observed in quasars (Hardcastle et al. 2009), and therefore exceeds by orders of magnitude the non-stellar nuclear optical-UV continuum in 4C+29.30 estimated by van Breugel et al. (1986). Yet it is in agreement with the required photoionizing flux for the observed equivalent width (EW) of the [OIII] emission-line in the extended emission-line region (a total required luminosity of the order of $\sim 10^{43} \text{ erg s}^{-1}$). van Breugel et al. (1986) excluded collisional ionization of the line-emitting gas given the observed line ratios and speculated on the source of the ionizing photons. Our new results imply that the AGN can provide the required energy to efficiently photo-ionize the extended emission-line region gas. Further investigations of the nature of the AGN buried in the center of 4C+29.30 are given in Sobolewska et al. (2012).

5.2. Broad-band Emission of the Jet

The one-sided radio jet of 4C+29.30 extends from the core to the south beyond the host galaxy and portions of it were detected in our deep *Chandra* image. Excluding the hotspot and core regions, a total radio luminosity of the jet is roughly $\sim 3 \times 10^{40} \text{ erg s}^{-1}$ (van Breugel et al. 1986). The X-ray spectrum is best modeled by an unabsorbed power-law continuum with a relatively large photon index of $\Gamma = 2.2 \pm 0.2$ resulting in a total X-ray luminosity of $\sim 3 \times 10^{40} \text{ erg s}^{-1}$, i.e., comparable to the jet radio luminosity. Therefore the observed X-ray emission is most likely non-thermal in origin, although thermal scenarios cannot be definitively excluded. That is because the jet X-ray emission is relatively faint, and hence we were forced to extract the spectrum over a relatively large extraction region. This average spectrum may be over-simplified since there are several ‘blobs’ or ‘patches’ of diffuse X-ray radiation scattered across the entire galaxy, and there is a non-negligible probability that a few such blobs would fall into this extraction region. Indeed, the jet’s X-ray morphology

consists of several isolated knots, and it is unclear whether there is any continuous low-surface brightness emission associated with the inter-knot regions (see Figure 8). The only sign of possible continuous X-ray emission aligned with the radio jet can be found in the vicinity closest to the core. However, there is a similar X-ray feature extending on a similar scale in the opposite direction from the core (to the north) and both features coincide with the known emission-line filaments which indicate the presence of a warm medium (van Breugel et al. 1986).

We note that our *Chandra* image may not be deep enough for a detection of the continuous X-ray jet emission. For example, in the case of the X-ray jet of Centaurus A (Hardcastle et al. 2003), there are many surface brightness enhancements embedded in a *faint* diffuse continuous emission (less than $\sim 10\%$ of the knots’ peaks). Many of these X-ray enhancements (though not all) have corresponding radio knots, and some of them also show offsets between the radio and X-ray peak brightnesses. In 4C+29.30, the limits to the inter-knot X-ray emission are of the order of 30 – 40% of the knots’ peaks. It is then possible that the jet X-ray diffuse emission is present but just below our detection limits and we are only able to detect X-ray knots.

We present a zoomed-in X-ray image of the jet overlaid with the radio contours at two different frequencies in Figure 8. The lower-resolution 1.4 GHz radio map shows a continuous and slowly expanding outflow flaring at the position of the southern hotspot. The higher-resolution 5 GHz radio map reveals instead a very knotty structure, with the innermost 4.3''-scale (or 5 kpc-long) linear feature terminating at the position of the X-ray enhancement located at the boundary of the 1.4 GHz jet. An isolated 5 GHz knot is present further away ($\sim 8''$ from the core), and *downstream* of the strongest X-ray peaked bright feature. Some faint enhancements in the X-ray emission are seen all along the radio jet further downstream up to the terminal hotspot where both the radio and X-ray emission peaks are well-aligned.

We cannot exclude some significant thermal contribution to the jet X-ray emission spectrally given the limited quality of the current data. However, in the case of a non-thermal origin for the bulk of the detected jet X-rays, two main processes can be invoked – synchrotron emission from high-energy relativistic electrons and the inverse Compton (IC) process involving low-energy particles only. There is strong evidence for the synchrotron origin of the X-ray emission in all FRI jets detected by *Chandra* (see Harris & Krawczynski 2006, and references therein) in general, including the Centaurus A radio galaxy (Kataoka et al. 2006; Worrall et al. 2008; Goodger et al. 2010). The synchrotron process has also been advocated for the X-ray jets in some FRII sources, such as Pictor A and 3C 353 (e.g., Hardcastle & Croston 2005; Kataoka et al. 2008). The X-ray photon index and luminosity, and the radio-to-X-ray flux ratio inferred for the 4C+29.30 jet are similar to those established for the other FRI objects, supporting the synchrotron interpretation also in this case.

In the synchrotron model, the Lorentz factors of the X-ray emitting electrons in the jet need to be as high as $\gamma \simeq \frac{1}{2} \delta^{-1/2} (\nu/10^{18} \text{ Hz})^{1/2} (B/\mu\text{G})^{-1/2} \sim 10^8$, for the

⁵ <http://heasarc.nasa.gov/docs/swift/results/bs58mon/>

equipartition magnetic field, $B \simeq 30 \mu\text{G}$, and the expected jet bulk Doppler factor, $\delta \sim a \text{ few}$. Stawarz & Ostrowski (2002) argued that 100 TeV-energy electrons could be produced by turbulent acceleration within the whole jet volume but especially at the jet boundaries where the interactions between the radio jet and the ISM can generate substantial turbulence (De Young 1986). There is strong observational evidence for such interactions to take place in 4C+29.30 and in the other low-power FRI systems in general. Electrons accelerated in this way could then be compressed by shocks at the positions of the knots.

Although, the synchrotron process is likely responsible for the jet X-rays, the IC scenario, favored by many authors in the case of powerful and X-ray-bright quasar jets (Tavecchio et al. 2000; Celotti et al. 2001), remains a formal possibility. There are several sources of seed photons for the IC scattering located at tens of kpc distances from the nucleus: (1) the cosmic microwave background (CMB), (2) starlight of the elliptical host (Stawarz et al. 2003; Hardcastle & Croston 2011); and (3) the beamed emission of the misaligned blazar core (Celotti et al. 2001; Migliori et al. 2012). The relevance of different photon fields depends on the velocity structure of the jet, while the resulting X-ray IC spectrum reflects the energy spectrum of the low-energy tail of the electron distribution (Harris & Krawczynski 2006). In this regard, one challenge to the IC hypothesis is that the observed spectral index of the jet-related X-ray emission in 4C+29.30 is larger than the spectral index of the jet radio continuum ($\alpha_r \simeq 0.8$; see van Breugel et al. 1986; Jamrozy et al. 2007). This is because the higher-energy electrons involved in producing synchrotron radio emission are not expected to be characterized by a flatter spectrum than the low-energy electrons inverse-Compton upscattering starlight/nuclear photons to the X-ray frequency range.

We conclude that the synchrotron scenario for the jet X-ray emission is the most likely option, even though some contribution due to the IC scattering of the starlight or of the blazar emission illuminating the jet from behind, or even a thermal origin of some fraction of the detected X-ray flux, cannot be excluded. A more in-depth understanding of the broad-band emission of various jet features in the source would however require more detailed modeling than considered here.

5.3. Hotspots and the Structure of the Outflow

In Figure 9 we show the radio and X-ray profiles along the radio source axis (P.A. = 24° ; here, the bulk of the AGN core emission is absorbed, and hence the X-ray core peak in the figure is dominated by the soft unabsorbed component). The emission at the two frequencies appears correlated, with the brightest radio and X-ray peaks aligned. The characteristic double structures of the radio features noted first by van Breugel et al. (1986) for the brightest knots in the radio jet and the hotspot regions can easily be seen in the radio profile. Note that the brighter peaks in these doubles are always located upstream of the outflow and that the X-ray counterparts have only been detected for these upstream features. In the observed profiles, the radio flux asymmetry between the prominent southern hotspot and the counter-hotspot to the north is also evident and this asymmetry is followed

in the X-rays.

Positional offsets between X-ray and radio peaks (with the X-ray peaks located upstream relative to the radio ones) and double structures of radio knots in general, have been seen in large-scale jets observed by *Chandra*, e.g., the cases of Centaurus A (Hardcastle et al. 2003), PKS 1127–145 (Siemiginowska et al. 2007), and 3C 353 (Kataoka et al. 2008). The origin of such offsets is still debated. Kataoka et al. (2008) suggested that such a morphology cannot be linked to stationary jet features (like nozzles of reconfinement shocks, for example), but instead could be due to moving portions of the plasma generated by the central engine during epochs of enhanced activity. Kataoka et al. further speculated that a complex double-shock structure may form as a result of the interaction between the two phases of the ejecta, with the reverse shock (propagating within the faster portion of the jet) being associated with the peak of the X-ray emission. This scenario may also possibly account for the properties of the 4C+29.30 jet and hotspots. If so, it is also of particular relevance for understanding the intermittent/modulated jet activity in this source (see discussion in Jamrozy et al. 2007).

The non-thermal (synchrotron, in particular) character of the X-ray emission of the southern hotspot advocated by Tavecchio et al. (2005) and supported by our spectral analysis (Section 4) fits the above model well. However, a possible thermal origin of the X-ray emission associated with the northern hotspot (on the counter-jet side) would then be puzzling. There have only been a few detections of thermal X-ray emission from the hotspots of powerful radio sources. In these cases, the emission was apparently enhanced by interactions between a radio jet and dense ISM clouds (Ly et al. 2005; Young et al. 2005). Indeed, the northern hotspot of 4C+29.30 coincides with the region of a significant amount of observed line-emitting gas, so may be an example of such a relatively rare phenomenon. But then the question remains why the X-ray peak brightness coincides with the upstream radio peak rather than with the outer (downstream) one. On the other hand, the soft X-ray spectrum of the northern hotspot may be alternatively described by the high-energy tail of the synchrotron continuum shaped by severe aging due to radiative losses of the underlying electron energy distribution. The spectral asymmetry between the southern and the northern hotspots could then possibly be related to the brightness asymmetry, and hence accounted for by relativistic effects (difference in relativistic beaming of the plasma at the reverse shocks on the jet and the counter-jet sides, light-travel effects, etc.) in the framework of the modulated jet activity scenario.

Even more likely, the differences in the local ISM between the regions north and the south of the nucleus could lead to distinctive source morphologies in these two directions of the outflow. The radio jet extending towards the south implies a possibly less disturbed outflow than the one to the north characterized by enhanced optical emission features due to interaction between the radio source and the dense medium (van Breugel et al. 1986). Such environmental differences were observed in other galaxies, although very high signal-to-noise data from deep *Chandra* observations were required to accurately determine the

nature of the X-ray emission as was performed for Centaurus A (Kraft et al. 2009; Croston et al. 2009). Interestingly, the very recent numerical simulations by Gaibler et al. (2011) confirm that interactions of bi-polar relativistic jets with the asymmetrically distributed multi-phase ISM can indeed result in an asymmetric morphology of the entire system, with the jet that propagates into the denser environment being restrained (at least for some time), and affecting at the same time the line-emitting clouds themselves in various ways. Future X-ray and other multi-waveband observations of 4C+29.30 are needed to fully understand the structure of the outflows and the two hotspots in the source.

5.4. Diffuse X-ray Features

In addition to the core, jet, and hotspots, our *Chandra* image reveals diffuse X-ray emission covering large parts of the galaxy and extending beyond the radio-emitting plasma. Some structures correlate with the extended emission-line region while others might be related to a recent merger event. For example, the two X-ray filaments perpendicular to the radio axis and extending from the core toward the SE and NW directions (HBranch and HBranchS regions in Figure 2) seem to be aligned with colder gas mixed with the dust seen in the archival optical images of the host galaxy, resembling the famous dust lane in the Centaurus A galaxy (Israel 1998). On the other hand, these two filaments may also be related to the jet activity. In particular, they may be a signature of gas compressed by the expanding lobes to form a quasi-linear structure perpendicular to the jet axis. Similar structures has been seen in Cygnus A (Wilson et al. 2006), although the horizontal structures (named ‘cold belts’ by Wilson et al. 2006) were not as straight as observed in 4C+29.30.

The diffuse X-ray structures seen to the north of the nucleus overlap with the clouds of line-emitting gas associated predominantly with the boundaries of the counter-lobe (van Breugel et al. 1986). Our spectral analysis indicate that the X-ray emission of these diffuse components is most likely thermal, with gas temperatures ranging from $\simeq 0.4$ keV up to $\simeq 0.6$ keV (see Table 5), with the possible exception of the southern regions located around the radio lobe downstream of the hotspot, for which either a non-thermal contribution or higher gas temperatures ($\simeq 0.8$ keV) remain valid options.

Given the normalization in the best-fit thermal model and the fixed emitting volumes (assuming 1 kpc depths for their third dimensions), we estimated the densities of the hot X-ray emitting gas in different regions (see Table 6). These densities vary roughly between $n_e \sim 0.02 \text{ cm}^{-3}$ in the southern regions, and $\sim 0.2 \text{ cm}^{-3}$ around the center and in the northern regions. It is interesting to note that the denser material is located in the regions with prominent optical line emission. The estimated values are consistent with the densities of hot gas found in other elliptical galaxies located in poor groups (Mathews & Brighenti 2003). 4C+29.30 might be located in such a group. We checked the NED for known galaxies located within 20 arcmin (~ 1 Mpc) of 4C+29.30 and with the velocities within $\pm 1000 \text{ km s}^{-1}$, so close enough to be possibly associated with a group. Only 4 galaxies with known redshifts met these selection criteria. One galaxy is closer

than $\pm 500 \text{ km s}^{-1}$ and only ~ 4.5 arcmin away, so possibly indicative of a group. Future observations are needed to confirm this conclusion.

The average pressures of the hot X-ray emitting gas are, $p_{\text{th}} \simeq 2 n_e kT \lesssim 10^{-10} \text{ dyne cm}^{-2}$ (see Table 6 for the pressure values of the individual features). This pressure is then comparable to/lower than the minimum non-thermal pressures of the jet, hotspots and the lobes (all estimated assuming energy equipartition between the radio-emitting electrons and the magnetic field), as well as the pressure of the line-emitting clouds calculated by van Breugel et al. (1986), i.e., $\sim 10^{-10} - 10^{-9} \text{ dyne cm}^{-2}$. We note that the pressure estimates for the line-emitting clouds are rather uncertain, and that our calculations assumed one size for the depth of all the analyzed regions, while van Breugel et al. used different scales for different components. Also, the minimum pressure calculations do not take into account the possible contribution of non-radiating particles (cosmic-ray protons in particular) to the jet/lobes’ pressure (see e.g. Dunn & Fabian 2004).

We conclude that it is most likely that the expanding radio source in 4C+29.30 is slightly overpressured with respect to the ambient medium (i.e., the hot ISM component), but it is likely in pressure equilibrium with the denser clouds of the colder material emitting the optical lines. We also note that van Breugel et al. (1986) found a velocity structure of the gas along the jet with increasing velocity towards the outer regions of the galaxy. The outermost gas is outflowing with velocities of $\gtrsim 500 \text{ km s}^{-1}$ exceeding the escape velocity for the host galaxy. The largest velocities (and the broadest emission lines) were found at the boundaries of the radio lobes and hotspots. Thus it is natural to conclude that the entire outflow is driven by the jets.

5.5. Shocks

The analysis of our X-ray data and the above pressure estimates also indicate that not only the colder line-emitting gas but also the hot X-ray emitting gas can be pushed out by the expanding radio-emitting plasma. The process may be accompanied by the formation of weak shocks around the lobes, as witnessed in several other analogous systems (such as Centaurus A, M 87, or NGC 1275; e.g., Croston et al. 2009; Million et al. 2010; Fabian et al. 2011, respectively). The shocks should then compress and heat the surrounding X-ray emitting gas and this may be the origin of the slightly hotter diffuse emission observed around the southern lobe of 4C+29.30.

We can estimate the Mach number of a shock which could heat this southern region. Assuming the standard shock jump condition, one gets the temperature jump:

$$\frac{T_+}{T_-} = \frac{[2\hat{\gamma}\mathcal{M}^2 - (\hat{\gamma} - 1)] [(\hat{\gamma} - 1)\mathcal{M}^2 + 2]}{(\hat{\gamma} + 1)^2 \mathcal{M}^2}, \quad (1)$$

where T_+ and T_- are the downstream and upstream gas temperatures, respectively, $\mathcal{M} \equiv v/c_s$ is the Mach number (as measured in upstream region), and the adiabatic index of the gas (assumed to be the same for the upstream and downstream medium) is $\hat{\gamma} = 5/3$, as appropriate for a non-relativistic fluid. For the observed temperatures of 0.5 keV for the ambient medium and 0.8 keV for the hotter component, the resulting Mach number reads as $\mathcal{M} = 1.6$. This

is a very reasonable Mach number and such weak shocks have been discovered in radio galaxies located in clusters of galaxies, such as Hydra A, Cygnus A, and Perseus A (Nulsen et al. 2005; Wilson et al. 2006; Fabian et al. 2006, respectively). However, a much stronger shock was associated with the southern lobe of Centaurus A ($\mathcal{M} \simeq 8$; Croston et al. 2009). Also, slightly higher Mach numbers ($\mathcal{M} \simeq 4$) have been claimed for the shocks driven by the radio structures expanding in the group environments of a low-power FRI radio galaxy NGC 3801 and a Seyfert galaxy Markarian 6, albeit at smaller scales ($\lesssim 10$ kpc; see Croston et al. 2007; Mingo et al. 2011, respectively).

We can check the velocity of the shock since we determined the temperature and density of the different regions in our X-ray data. For a $kT = 0.5$ keV, the sound velocity in the upstream medium is $c_s = \sqrt{\gamma kT/\mu m_p} \simeq 360 \text{ km s}^{-1}$, assuming a non-relativistic gas ($\gamma = 5/3$) and the mean molecular weight of the gas $\mu = 0.6$. A $\mathcal{M} \simeq 1.6$ shock propagating within the gas characterized by this sound velocity implies the radio lobes driving the shocks have an expansion velocity, $v_{\text{exp}} = \mathcal{M} \times c_s \simeq 580 \text{ km s}^{-1}$. This is in excellent agreement with the highest velocity measured for the line-emitting gas $\gtrsim 500 \text{ km s}^{-1}$ and strongly supports the idea that feedback is operating in this galaxy.

The implied shock velocity of 580 km s^{-1} can be used to estimate a size for the region influenced by the shock during the source lifetime. Assuming the source dynamical age of ~ 33 Myr (Jamrozy et al. 2007), the calculated source size is consistent with the extension of the SLOB (~ 20 kpc). We conclude that during the lifetime of the source, the whole SLOB region could indeed be shock-heated.

We also comment on the northern X-ray emission region we identified as EArm. This structure is located outside and along the eastern boundary of the northern radio lobe and is slightly offset from the strongest radio emission. Interestingly, van Breugel et al. (1986) reported a large velocity jump (by $\sim 300 \text{ km s}^{-1}$) in the optical-line emitting gas in this region. In an X-ray surface brightness profile across EArm (Figures 10 and 11), we found that the surface brightness increases by a factor of $\sim 2 - 2.5$ at the location of EArm over the projected width of ~ 3 kpc. Although it is tempting to associate the surface brightness increase as due to shock heating and compressing the background plasma, we were unable to constrain the temperature profile in this region in our current data. However, we note that EArm could be similar to the X-ray emission observed at the boundary of the southern lobe of Centaurus A (Croston et al. 2009) where the evidence for the shock exists in a deep *Chandra* image. The shock in Centaurus A is resolved on parsec scales ($1'' \sim 18$ pc) and the change in the surface brightness is measured across a ~ 1 kpc region. The EArm ‘width’ is much larger, and the enhancement covers about 3 kpc, but its morphology seems to relate this structure to the radio lobe. Future higher signal-to-noise data are necessary to properly assess the presence of a shock in the EArm feature.

We conclude that signatures of weak shocks due to an

expanding radio source are present in the X-ray data. The radio-emitting outflow in 4C+29.30 interacts therefore clearly with the ambient medium, not only accelerating denser and colder optical-line emitting clouds present within the ISM as found before, but also heating and displacing the warm phase of its gaseous environment, thus providing strong evidence for a complex jet-related feedback in a post-merger galaxy. We note that interactions of a relativistic magnetized jet with a *multi-phase* ISM are rarely subjected to detailed numerical simulations (but see Krause & Alexander 2007; Sutherland & Bicknell 2007; Wagner & Bicknell 2011), even though the problem is particularly relevant in the context of high-redshift ($z > 1$) radio galaxies.

5.6. Source Energetics

The intrinsic luminosity of the nucleus of 4C+29.30 of $\sim 10^{45} \text{ erg s}^{-1}$ implies an accretion power of order $\sim 10^{46} \text{ erg s}^{-1}$, assuming a standard value of 10% for the radiative efficiency. It also implies a mass of the central supermassive black hole that exceeds $\sim 10^8 M_\odot$. The observed non-thermal X-ray luminosities of the jet and hotspots put a strict lower limit on the source radio power of $> 10^{41} \text{ erg s}^{-1}$.

The minimum jet power can also be calculated from the radio measurements. The total energy of the southern radio lobe (tail) calculated under the equipartition condition is equal to $E_\ell \sim 10^{57} \text{ erg}$.⁶ The north and south radio structures (excluding the southern tail) have similar minimum energy estimates of $\sim 10^{57} \text{ erg}$. If we now take the age of the radio source, $t_j \sim 30$ Myr (Jamrozy et al. 2007), we can obtain a lower limit to the jet kinetic energy required to power the radio lobes of $L_j \sim E_\ell/t_j \sim 10^{42} \text{ erg s}^{-1}$. Interestingly, this is also the minimum power needed for heating the surrounding thermal gas required by our *Chandra* observations. The thermal energy in the diffuse X-ray emitting component is $E_{\text{th}} \sim 10^{56} - 10^{57} \text{ erg}$, which is also in agreement with the minimum energy estimates for the radio structures given above and would require a continuous energy supply of $\sim 10^{41} - 10^{42} \text{ erg s}^{-1}$ over the radio source lifetime.

A total ionized Hydrogen mass in the line-emitting clouds of 4C+29.30 estimated by van Breugel et al. (1986) is about $\sim 10^6 M_\odot$ and their total kinetic energy is of order $E_{\text{kin}} \sim 10^{54} \text{ erg}$. This is much smaller than the total energy deposited by the jets within the lobes. Thus we can conclude that only a small fraction of the available jet power is needed to drive the gaseous optical outflow, while a much higher fraction ($> 10\%$) of the total jet power ($\sim 10^{56} \text{ erg}$) is used to heat the surrounding medium to the X-ray temperatures (> 0.1 keV).

We can also compare the energy stored in the outer lobes formed during the previous outburst of the radio source to the current jet power. Approximating the outer lobes as a cylinder with a height $h = 640$ kpc and a radius $r = h/4$, the source volume is $V = \pi r^2 h$. Assuming the minimum energy magnetic field $B = 0.7 \mu\text{G}$ ($U_B = B^2/8\pi$) and lifetime $t_{\text{out}} \geq 200$ Myr given by Jamrozy et al. (2007), the required jet power is equal to $L_j \sim 2U_B V/t_{\text{out}} \sim 10^{43} \text{ erg s}^{-1}$. This is a lower limit to

⁶ We note that the value reported by van Breugel et al. (1986) in their Table 4B, is 2 orders of magnitude higher, which we believe is an error. Here, we assumed $40''$ for the third dimension in calculating the volume (i.e. the same as in van Breugel et al. (1986)) and also estimated the equipartition magnetic field of $3.4 \mu\text{G}$ for the observed flux density of 0.26 Jy at 1.4 GHz .

the jet power in the previous outburst as the duration of the active phase might be shorter than t_{out} . However, this jet power indicates that the previous outburst of the jet activity might have been more powerful than the current one in agreement with the powers derived for other double-double radio sources.

6. SUMMARY AND CONCLUSIONS

We presented the results of our new deep ($\simeq 300$ ksec) *Chandra* X-ray observations of the nearby radio galaxy 4C+29.30. These X-ray data brought a new dimension to studies of radio source impact on the ISM and enabled a detailed analysis of the processes associated with the feedback.

The main results of our studies can be summarized as follows:

- The new *Chandra* image of 4C+29.30 revealed a complex X-ray morphology with different features on the same scale (~ 50 kpc) as the radio (inner) source and the extended optical emission-line region. This indicates complex interactions between radio-, optical line-, and X-ray-emitting plasmas.
- The nucleus of the galaxy is surprisingly powerful in X-rays ($\sim 10^{44}$ erg s $^{-1}$) and heavily obscured by a significant amount of matter in-falling onto the center (also indicated by HI absorption lines). This infall may be related to the feeding of the nucleus and triggering the current jet activity. The nuclear emission is sufficiently luminous to photo-ionize the whole extended emission line region. In this respect, contrary to estimates based on the optical continuum only (van Breugel et al. 1986), no other source of ionizing photons or other processes of ionization is needed.
- The X-ray emission of the jet and the hotspots seems to be particularly complex, with different and distinct emission components, both ther-

mal and non-thermal (synchrotron and/or inverse-Compton). Although we favor the synchrotron scenario for the jet and the hotspots, more definitive statements would require detailed modeling and higher quality multi-wavelength data in the future.

- A significant fraction of the jet energy (jet power, $L_j \sim 10^{42}$ erg s $^{-1}$) goes into heating the surrounding gas and the X-ray data support the heating of the ambient medium via weak shocks with the Mach number, $\mathcal{M} = 1.6$. Only a small amount of the jet power is needed to accelerate clouds of colder material which are dragged along the outflow.

Our study provides evidence for the AGN impact on the host galaxy ISM and feedback processes. We show that a relatively large amount of the energy generated by an accreting SMBH is dissipated by the outflow and used to heat the ISM. A smaller fraction of the energy drives the colder gas out from the central regions and also heats up the medium. Both processes can lead to a limited fuel supply and starving the SMBH, and finally stopping its growth.

ACKNOWLEDGMENTS

The authors thank the anonymous referee for insightful comments and Małgorzata Sobolewska, Ralph Kraft, and Dharam Vir Lal for fruitful discussion. L.S. is grateful for the support from Polish MNiSW through the grant N-N203-380336. M.J. was supported by MNiSW funds for scientific research in years 2009-2012 under the contract No. 3812/B/H03/2009/36. Work at NRL is sponsored by NASA DPR S-15633-Y. This research has made use of data obtained by the *Chandra* X-ray Observatory, and *Chandra* X-ray Center (CXC) in the application packages CIAO, ChIPS, and Sherpa. This research is funded in part by NASA contract NAS8-39073. Partial support for this work was provided by the *Chandra* grant GO0-11133X and XMM-Newton grant NNX08AX35G.

REFERENCES

- Baumgartner, W.H. et al. 2010, ApJS, submitted
 Canosa, C. M., Worrall, D. M., Hardcastle, M. J., & Birkinshaw, M. 1999, MNRAS, 310, 30
 Cash, W. 1979, ApJ, 228, 939
 Celotti, A., Ghisellini, G., & Chiaberge, M. 2001, MNRAS, 321, L1
 Chandola, Y., Saikia, D. J., & Gupta, N. 2010, MNRAS, 403, 269
 Cheung C. C., 2004, PhD Thesis, Brandeis University
 Chiang, J. 2002, ApJ, 572, 79
 Croston, J. H., Kraft, R. P., & Hardcastle, M. J. 2007, ApJ, 660, 191
 Croston, J. H., Kraft, R. P., Hardcastle, M. J., et al. 2009, MNRAS, 395, 1999
 Croton, D. J., et al. 2006, MNRAS, 365, 11
 De Young, D. S. 1986, ApJ, 307, 62
 Dickey, J. M., & Lockman, F. J. 1990, ARA&A, 28, 215
 Dunn, R. J. H., & Fabian, A. C. 2004, MNRAS, 355, 862
 Fabian, A. C., Sanders, J. S., Ettori, S., et al. 2000, MNRAS, 318, L65
 Fabian, A. C., Sanders, J. S., Taylor, G. B., et al. 2006, MNRAS, 366, 417
 Fabian, A. C., Sanders, J. S., Allen, S. W., et al. 2011, MNRAS, 417, 172
 Freeman, P., Doe, S., & Siemiginowska, A. 2001, Proc. SPIE, 4477, 76
 Fruscione, A., et al. 2006, Proc. SPIE, 6270, 60
 Gaibler, V., Khochfar, S., & Krause, M. 2011, MNRAS, 411, 155
 Gambill, J. K., Sambruna, R. M., Chartas, G., Cheung, C. C., Maraschi, L., Tavecchio, F., Urry, C. M., & Pesce, J. E. 2003, A&A, 401, 505
 Goodger, J. L., Hardcastle, M. J., Croston, J. H., et al. 2010, ApJ, 708, 675
 Gupta, N., Salter, C. J., Saikia, D. J., Ghosh, T., & Jeyakumar, S. 2006, MNRAS, 373, 972
 Hardcastle, M. J., & Croston, J. H. 2005, MNRAS, 363, 649
 Hardcastle, M. J., Evans, D. A., & Croston, J. H. 2006, MNRAS, 370, 1893
 Hardcastle, M. J., Kraft, R. P., Sivakoff, G. R., et al. 2007, ApJ, 670, L81
 Hardcastle, M. J., Evans, D. A., & Croston, J. H. 2009, MNRAS, 396, 1929
 Hardcastle, M. J., & Croston, J. H. 2011, MNRAS, 415, 133
 Hardcastle, M. J., Worrall, D. M., Kraft, R. P., et al. 2003, ApJ, 593, 169
 Harris, D. E., & Krawczynski, H. 2006, ARA&A, 44, 463
 Holt, J., Tadhunter, C. N., & Morganti, R. 2008, MNRAS, 387, 639
 Holt, J., Tadhunter, C. N., Morganti, R., & Emonts, B. H. C. 2011, MNRAS, 410, 1527
 Holt, J., Tadhunter, C. N., & Morganti, R. 2009, MNRAS, 400, 589
 Israel, F. P. 1998, A&A Rev., 8, 237
 Jamroz, M., Konar, C., Saikia, D. J., Stawarz, L., Mack, K.-H., & Siemiginowska, A. 2007, MNRAS, 378, 581
 Kataoka, J., Stawarz, L., Aharonian, F., et al. 2006, ApJ, 641, 158
 Kataoka, J., Stawarz, L., Harris, D. E., et al. 2008, ApJ, 685, 839

- Kelly, B. C., Bechtold, J., Siemiginowska, A., Aldcroft, T., & Sobolewska, M. 2007, *ApJ*, 657, 116
- Kim, D.-W. 2012, *Astrophysics and Space Science Library*, 378, 121
- Kraft, R. P., et al. 2009, *ApJ*, 698, 2036
- Kraft, R. P., Nulsen, P. E. J., Birkinshaw, M., et al. 2007, *ApJ*, 665, 1129
- Krause, M., & Alexander, P. 2007, *MNRAS*, 376, 465
- Ly, C., De Young, D. S., & Bechtold, J. 2005, *ApJ*, 618, 609
- Mathews, W. G., & Brighenti, F. 2003, *ARA&A*, 41, 191
- McCarthy, P. J., Baum, S. A., & Spinrad, H. 1996, *ApJS*, 106, 281
- McNamara, B. R., & Nulsen, P. E. J. 2007, *ARA&A*, 45, 117
- Merloni, A., & Heinz, S. 2008, *MNRAS*, 388, 1011
- Migliori, G., Siemiginowska, A., & Celotti, A. 2011, *ApJ*, in press
- Million, E. T., Werner, N., Simionescu, A., et al. 2010, *MNRAS*, 407, 2046
- Mingo, B., Hardcastle, M. J., Croston, J. H., et al. 2011, *ApJ*, 731, 21
- Morganti, R. 2010, *PASA*, 27, 463
- Morganti, R., Oosterloo, T., Struve, C., & Saripalli, L. 2008, *A&A*, 485, L5
- Morganti, R., Tadhunter, C. N., & Oosterloo, T. A. 2005, *A&A*, 444, L9
- Nelder, J. A. & Mead, R. 1965, *Computer Journal*, vol7, pp.308-313
- Nesvadba, N. P. H., Lehnert, M. D., De Breuck, C., Gilbert, A., & van Breugel, W. 2007, *A&A*, 475, 145
- Nulsen, P. E. J., McNamara, B. R., Wise, M. W., & David, L. P. 2005, *ApJ*, 628, 629
- O'Dea, C. P., de Vries, W. H., Koekemoer, A. M., et al. 2002, *AJ*, 123, 2333
- Ostorero, L., Moderski, R., Stawarz, L., et al. 2010, *ApJ*, 715, 1071
- Owen, F. N., Eilek, J. A., & Kassim, N. E. 2000, *ApJ*, 543, 611
- Refsdal, B. et al. 2009, in *Proceedings of the 8th Python in Science conference (SciPy 2009)*, G. Varoquaux, S. van der Walt, J. Millman (Eds.), pp. 51-57
http://conference.scipy.org/proceedings/SciPy2009/paper_8
- Saikia, D. J., Gupta, N., & Konar, C. 2007, *MNRAS*, 375, L31
- Saikia, D. J., & Jamroz, M. 2009, *Bulletin of the Astronomical Society of India*, 37, 63
- Sambruna, R. M., Gambill, J. K., Maraschi, L., Tavecchio, F., Cerutti, R., Cheung, C. C., Urry, C. M., & Chartas, G. 2004, *ApJ*, 608, 698
- Siemiginowska, A., Stawarz, L., Cheung, C. C., et al. 2007, *ApJ*, 657, 145
- Siemiginowska, A., Burke, D. J., Aldcroft, T. L., Worrall, D. M., Allen, S., Bechtold, J., Clarke, T., & Cheung, C. C. 2010, *ApJ*, 722, 102
- Singh, V., Shastri, P., & Risaliti, G. 2011, *A&A*, 533, A128
- Silk, J., & Rees, M. J. 1998, *A&A*, 331, L1
- Sobolewska, M. A., Siemiginowska, A., Życki, P. T. 2004a, *ApJ*, 608, 80
- Sobolewska, M. A., Siemiginowska, A., Życki, P. T. 2004b, *ApJ*, 617, 102
- Sobolewska, M. A., Siemiginowska, A., & Gierliński, M. 2011, *MNRAS*, 413, 2259
- Sobolewska, M. A., et al. 2011, in preparation.
- Sobolewska, M. A., Gierliński, M., & Siemiginowska, A. 2009, *MNRAS*, 394, 1640
- Stawarz, L., & Ostrowski, M. 2002, *ApJ*, 578, 763
- Stawarz, L., Sikora, M., & Ostrowski, M. 2003, *ApJ*, 597, 186
- Sutherland, R. S., & Bicknell, G. V. 2007, *ApJS*, 173, 37
- Tadhunter, C. 2007, *New Astronomy Reviews*, 51, 153
- Tavecchio, F., Maraschi, L., Sambruna, R. M., & Urry, C. M. 2000, *ApJ*, 544, L23
- Tavecchio, F., Cerutti, R., Maraschi, L., Sambruna, R. M., Gambill, J. K., Cheung, C. C., & Urry, C. M. 2005, *ApJ*, 630, 721
- van Breugel, W. J. M., Heckman, T. M., Miley, G. K., & Filippenko, A. V. 1986, *ApJ*, 311, 58
- Wagner, A. Y., & Bicknell, G. V. 2011, *ApJ*, 728, 29
- Wang, J., Fabbiano, G., Risaliti, G., Elvis, M., Mundell, C. G., Dumas, G., Schinnerer, E., & Zezas, A. 2010, *ApJ*, 719, L208
- Wang, J., Fabbiano, G., Risaliti, G., et al. 2011a, *ApJ*, 729, 75
- Wang, J., Fabbiano, G., Elvis, M., Risaliti, G., Mundell, C. G., Karovska, M., & Zezas, A. 2011b, *ApJ*, 736, 62
- Wilson, A. S., Smith, D. A., & Young, A. J. 2006, *ApJ*, 644, L9
- Worrall, D. M., et al. 2008, *ApJ*, 673, L135
- Young, A. J., Wilson, A. S., Tingay, S. J., & Heinz, S. 2005, *ApJ*, 622, 830

TABLE 1
CHANDRA OBSERVATIONS

OBSID	Exposure (ksec)	Date
11688	123.4	2010-2-19
11689	75.5	2010-2-25
12106	32.0	2010-2-18
12119	55.5	2010-2-23

TABLE 2
SPECTRAL REGIONS.

Name	Total Cts ^a 0.5-7 keV	Net Cts ^a 0.5-7 keV	Region Definition ^b
NLobe	319	275±19	ellipse(08:40:02.34,+29:49:14.63,0.1135',0.07073',0) -circle(08:40:02.61,+29:49:13.48,0.0267')
NLobe1	75	62±9	rotbox(08:40:02.925,+29:49:17.42,0.05308',0.12527',0)
NHspot	247	242±16	circle(08:40:02.613,+29:49:13.48,0.02673')
SHspot	558	553±24	circle(08:40:01.729,+29:48:47.04,0.02907')
SJet	126	110 ±12	rotbox(08:40:02.019,+29:48:54.20,0.041933',0.2033',31.7134)
SLobe	301	169±21	ellipse(08:40:02.110,+29:48:42.35,0.22604',0.102',12.9697) -circle(08:40:01.729,+29:48:47.04,0.0292')
SLobe1	145	97±14	circle(08:40:01.607,+29:48:43.77,0.0943') -circle(08:40:01.729,+29:48:47.04,0.0292')
Center	1097	1059±34	ellipse(08:40:02.341,+29:49:02.69,0.06631',0.10317',0) -circle(08:40:02.345,+29:49:02.61,0.021')
Total	3500	2574±66	rotbox(08:40:02.399,+29:49:01.14,0.635105',0.7768',0) -circle(08:40:02.345,+29:49:02.61,0.021') -circle(08:40:01.743,+29:48:46.95,0.0295') -circle(08:40:02.606,+29:49:13.66,0.0295')
EArm	124	92±12	pie(08:40:03.00,+29:49:12.27,0.047682',0.1256',123.322,266.705)
HBranch	340	238±21	rotbox(08:40:01.374,+29:49:14.02,0.122393',0.4380',311.166)
HBranchS	356	295±20	rotbox(08:40:02.776,+29:48:55.52,0.19036',0.16845',38.496)
Core	5328	5303±73	circle(08:40:02.345,+29:49:02.61,0.02083')
Core_ext	833	676±32	annulus(08:40:02.345,+29:49:02.61,0.0246',0.0754')

Note: ^a Total and background subtracted counts in each region in energies between 0.5 keV and 7 keV.

^b CIAO regions are given in J2000 and the arcmin units for the sizes.

TABLE 3
BEST-FIT MODEL PARAMETERS FOR THE NUCLEUS.

Component	Parameters ^a	Norm ^b [photons cm ⁻² s ⁻¹ keV ⁻¹]
Nucleus model – gal(bremss+abs*pow)		
Absorption	$N_H = 3.95^{+0.27}_{-0.33} \times 10^{23} \text{ cm}^{-2}$	
Power Law	$\Gamma = 1.70^{+0.38}_{-0.36}$	$1.26^{+1.48}_{-0.64} \times 10^{-3}$
Bremstrahlung	kT = $6.8^{+9.9}_{-2.5} \text{ keV}$	$4.2^{+0.5}_{-0.2} \times 10^{-6}$
Nucleus model – gal (apec+abs*pow)		
Absorption	$N_H = 4.37^{+0.17}_{-0.30} \times 10^{23} \text{ cm}^{-2}$	
Power Law	$\Gamma = 1.87^{+0.36}_{-0.34}$	$1.79^{+1.87}_{-0.88} \times 10^{-3}$
APEC ^c	kT = $9.6^{+10.0}_{-4.9}$ $A < 1.34$	$1.5^{+0.1}_{-0.3} \times 10^{-5}$
Nucleus model – gal (pow_soft+abs*pow)		
Absorption	$N_H = 3.93^{+0.17}_{-0.30} \times 10^{23} \text{ cm}^{-2}$	
Power Law	$\Gamma = 1.68^{+0.36}_{-0.34}$	$1.21^{+0.12}_{-0.60} \times 10^{-3}$
Soft Power Law	$\Gamma = 1.60^{+0.12}_{-0.12}$	$3.18^{+1.87}_{-0.88} \times 10^{-6}$
Background model – scale*gal(bremss+pow)		
Power Law	$\Gamma = -2.3^{+0.2}_{-0.2}$	$3.8^{+1.6}_{-1.2} \times 10^{-8}$
Bremsstrahlung	kT = $0.59^{+0.04}_{-0.04} \text{ keV}$	$2.57^{+0.27}_{-0.24} \times 10^{-5}$
Scales ^c	1.07±0.07 1.15±0.08 1.09±0.09	

NOTE – Components in model expression: gal - galactic absorption $N_H=3.98 \times 10^{20} \text{ cm}^{-2}$ - fixed in all models; abs - intrinsic absorption of the nucleus; power law - absorbed intrinsic power law component, absorbed; bremss - unabsorbed bremsstrahlung thermal emission; apec - unabsorbed APEC plasma model. ^a Uncertainties are 1σ for one interesting parameter. ^b A model normalization is given at 1 keV. ^c A - an abundance parameter in APEC model expressed in the Solar values. ^d Scale factors in respect to the data set 1.

TABLE 4
PARAMETERS OF POWER LAW MODEL FITS TO X-RAY SPECTRA OF VARIOUS REGIONS.

Region	N_H^a [10^{22} cm^{-2}]	Γ	Flux(0.5-2) ^b [$10^{-15} \text{ erg cm}^{-2} \text{ s}^{-1}$]	Flux(2-10) ^b [$10^{-15} \text{ erg cm}^{-2} \text{ s}^{-1}$]	Stat(Cash) ^c
NLobe	— 0.41 ^{+0.15} _{-0.14}	3.5 ^{+0.2} _{-0.2} 5.9 ^{+0.1} _{-0.1}	45.9±0.3 31.6±15.0	0.64±0.03 0.18±0.15	3527.26 3518.0
NLobe1	— < 0.15	2.16 ^{+0.28} _{-0.28} < 2.5	0.82±0.06 1.0±2.7	0.75±0.41 0.9±0.4	3082.28 3082.12
NHspot	— 0.33 ^{+0.11} _{-0.10}	3.34 ^{+0.16} _{-0.15} 5.0 ^{+0.7} _{-0.6}	4.09±0.16 16.8±6.9	0.66±0.06 0.03±0.02	3248.37 3237.69
SHspot	— 0.06 ^{+0.04} _{-0.04}	2.16 ^{+0.08} _{-0.08} 2.24 ^{+0.16} _{-0.15}	7.2±0.2 7.7±1.3	6.5±0.9 8.6±1.1	3849.86 3849.59
SJet	— < 0.08	2.2 ^{+0.2} _{-0.2} < 2.1	1.42±0.07 3.3±2.0	1.24±0.62 0.68±0.47	3279.82 3279.47
SLobe	— < 0.13	2.73 ^{+0.24} _{-0.23} < 2.8	2.5±0.1 3.6±1.9	0.97±0.50 0.60±0.3	3885.83 3885.77
SLobe1	— < 0.046	2.1 ^{+0.3} _{-0.3} < 2.0	1.18±0.06 18.6±9.7	1.18±0.66 < 0.4	3422.7 3421.85
Center	— < 0.001	1.15 ^{+0.06} _{-0.06} < 1.1	9.5±0.2 9.1±0.6	39.9±4.5 37.1±4.5	5377.53 5320.22
EArm	— 0.65 ^{+0.34} _{-0.30}	3.5 ^{+0.3} _{-0.3} 7.7 ^{+2.3} _{-2.1}	1.58±0.14 50.1±5.2	0.2±0.07 0.02±0.01	3198.87 3193.89
HBranch	— 0.60 ^{+0.22} _{-0.18}	3.5 ^{+0.2} _{-0.2} 7.6 ^{+1.5} _{-1.4}	2.6±0.2 98.0±39.8	0.45±0.01 0.04±0.03	3856.6 3845.09
HBranchS	— 0.53 ^{+0.17} _{-0.16}	3.0 ^{+0.2} _{-0.2} 6.3 ^{+1.2} _{-1.1}	4.21±0.47 58.2 ±17.0	1.09±0.21 0.15±0.09	3838.9 3829.35
Core_ext	— <0.002	2.5 ^{+0.2} _{-0.2} < 2.2	7.95±0.18 6.83±0.42	4.1±1.5 14.6±2.8	4422.43 4407.48

NOTE.- The first row for each regions shows the best fit model parameters for the absorption fixed at the Galactic column of $3.98 \times 10^{20} \text{ cm}^{-2}$. The second row shows the best fit absorption column for that region. Errors are 68% for one significant parameter and upper and lower limits are at 90%

^a Hydrogen equivalent absorption column in 10^{22} cm^{-2} . It was frozen in the first fit and thawed in the second fit for each region;

^b Model flux in the units of $10^{-15} \text{ erg cm}^{-2} \text{ s}^{-1}$; Errors calculated via simulations with `sample_energy_flux` in Sherpa.

^c degrees of freedom were equal to 3565 and 3564 for the model fit with a frozen and thawed absorption parameter respectively.

TABLE 5
PARAMETERS OF THERMAL MODEL FITS TO X-RAY SPECTRA OF VARIOUS REGIONS.

Region	N_H^a	kT^b	Abundance ^c	Norm ^d	Flux(0.5-2) ^e	Flux(2-10)) ^e	Stat (Cash) ^f
NLobe	-	0.45 ^{+0.05} _{-0.04}	-	10.84 ^{+2.19} _{-1.76}	4.47±0.46	0.15±0.03	3519.1
	0.157 ^{+0.090} _{-0.008}	0.33 ^{+0.09} _{-0.08}	-	33.19 ^{+0.08} _{-0.06}	7.02±0.22	0.05±0.01	3516.8
	-	0.64 ^{+0.10} _{-0.06}	0.06 ^{+0.03} _{-0.02}	13.4 ^{+3.7} _{-3.6}	4.2±0.4	0.20±0.05	3516.8
NLobe1	-	1.9 ^{+1.0} _{-0.5}	-	0.55 ^{+0.14} _{-0.11}	0.81±0.12	0.44±0.15	3081.8
	< 0.1	2.1 ^{+1.1} _{-0.7}	-	0.18 ^{+0.08} _{-0.05}	0.72±0.19	0.48±0.15	3081.7
	-	2.0 ^{+1.2} _{-0.6}	< 0.8	1.8 ^{+0.5} _{-0.4}	0.8±0.1	0.4±0.3	3086.9
NHspot	-	0.54 ^{+0.06} _{-0.04}	-	7.28 ^{+1.17} _{-1.15}	3.97±0.28	0.19±0.03	3240.9
	0.078 ^{+0.067} _{-0.058}	0.49 ^{+0.07} _{-0.06}	-	9.75 ^{+1.07} _{-0.08}	4.64±0.20	0.16±0.03	3240.5
	-	0.79 ^{+0.06} _{-0.06}	0.06 ^{+0.03} _{-0.02}	9.4 ^{+2.3} _{-1.7}	3.7±0.3	0.29±0.07	3233.9
SHspot	-	2.2 ^{+0.3} _{-0.2}	-	4.58 ^{+0.31} _{-0.28}	7.05±0.38	4.65±0.10	3855.7
	< 0.01	< 2.57	-	3.95 ^{+0.24} _{-0.28}	6.29±0.38	4.96±0.10	3850.0
	-	2.3 ^{+0.3} _{-0.2}	< 0.09	15.8 ^{+0.9} _{-1.0}	7.0±0.5	4.7±0.1	3860.2
SJet	-	2.1 ^{+0.9} _{-0.6}	-	0.91 ^{+0.18} _{-0.14}	1.37±0.07	0.84±0.17	3283.9
	< 0.022	< 2.6	-	< 1.7	1.22±0.07	0.96±0.19	3282.0
	-	2.3 ^{+0.9} _{-0.6}	< 0.13	3.1 ^{+0.6} _{-0.4}	1.4±0.2	0.9±0.7	3289.2
SLobe	-	0.80 ^{+0.21} _{-0.15}	-	2.82 ^{+0.78} _{-0.59}	2.41±0.13	0.31±0.08	3887.4
	< 0.042	< 1.1	-	2.08 ^{+0.27} _{-0.22}	2.09±0.13	0.39±0.08	3886.4
	-	0.9 ^{+0.2} _{-0.2}	< 0.03	8.9 ^{+2.3} _{-1.7}	2.4±0.3	0.4±0.2	3893.9
SLobe1	-	2.24 ^{+1.40} _{-0.74}	-	0.74 ^{+0.18} _{-0.13}	1.15±0.06	0.77±0.16	3424.6
	< 0.027	< 2.6	-	< 2.4	1.05±0.06	0.82±0.16	3423.7
	-	2.45 ^{+1.98} _{-0.75}	< 1.5	2.6 ^{+0.5} _{-0.7}	1.2±0.2	0.81±0.08	3430.6
Center ^g	-	0.53 ^{+0.13} _{-0.02}	-	19.9 ^{+13.9} _{-7.6}	9.7±0.5	35.7±7.1	4685.7
	< 19.71	0.63 ^{+0.08} _{-0.24}	-	15.7 ^{+7.3} _{-3.3}	10.4±0.6	33.5±6.8	4684.5
	-	18.7 ^{+4.8} _{-2.6}	> 4.6	15.1 ^{+0.9} _{-0.7}	10.2±1.1	33.1±3.1	5379.2
Total	-	0.59 ^{+0.03} _{-0.03}	-	51.38 ^{+4.17} _{-3.82}	31.2±1.6	1.9±0.1	1491.9
	< 0.006	< 0.74	-	< 34.24	26.8±1.6	2.8±0.1	1485.5
	-	0.78 ^{+0.03} _{-0.03}	0.04 ^{+0.01} _{-0.01}	91.5 ^{+6.4} _{-5.9}	29.8±1.1	2.6±0.3	1492.4
EArm	-	0.39 ^{+0.08} _{-0.06}	-	4.74 ^{+2.01} _{-1.40}	1.54±0.78	0.02±0.01	3195.6
	0.44 ^{+0.28} _{-0.20}	< 0.27	-	< 314.9	12.8±0.1	< 0.001	3190.8
	-	0.71 ^{+0.08} _{-0.16}	0.13 ^{+0.14} _{-0.08}	2.5 ^{+2.1} _{-1.0}	1.3±0.1	0.07±0.01	3192.7
HBranch	-	0.40 ^{+0.05} _{-0.04}	-	10.63 ^{+2.84} _{-2.19}	3.52±0.16	0.05±0.01	3845.3
	0.573 ^{+0.242} _{-0.177}	< 0.24	-	< 305.0	63.8±3.8	< 0.001	3832.5
	-	0.75 ^{+0.05} _{-0.06}	0.18 ^{+0.13} _{-0.07}	4.7 ^{+1.8} _{-1.6}	3.0±0.4	0.15±0.06	3832.9
HBranchS	-	0.51 ^{+0.06} _{-0.05}	-	8.19 ^{+1.66} _{-1.28}	4.15±0.21	0.16±0.03	3834.3
	0.327 ^{+0.114} _{-0.102}	0.27 ^{+0.11} _{-0.10}	-	< 121.0	15.7±1.6	0.03±0.01	3824.3
	-	0.75 ^{+0.06} _{-0.06}	0.09 ^{+0.04} _{-0.03}	8.4 ^{+2.1} _{-1.8}	3.8±0.4	0.25±0.06	3817.3
Core_ext	-	8.2 ^{+10.2} _{-2.7}	-	3.98 ^{+0.47} _{-0.88}	6.6±0.4	13.1±2.5	4515.1
	< 0.002	< 12.05	-	< 15.8	5.9±0.4	14.1±2.8	4472.9
	-	13.7 ^{+3.2} _{-1.3}	> 3.7	9.8 ^{+0.8} _{-0.5}	7.2±0.2	22.3±2.2	4766.5

NOTE.- The first row for each regions shows the best fit model parameters for the absorption fixed at the Galactic column of $3.98 \times 10^{20} \text{ cm}^{-2}$ and the abundance fixed at 0. The second row shows the best fit absorption column for that region. The third row shows the results of the model fit with abundance free and the absorption column fixed at the Galactic value. Errors are 68% for one significant parameter and upper and lower limits are at 90%.

^a Hydrogen equivalent absorption column in 10^{22} cm^{-2} ; ^b the temperature in keV; ^c metal abundances in terms of fraction of the Solar; ^d Norm in units of $10^{-6} \text{ photons cm}^{-2} \text{ s}^{-1}$; ^e Flux in the units of $10^{-15} \text{ erg cm}^{-2} \text{ s}^{-1}$; Errors calculated via simulations. ^f degrees of freedom were equal to 3565 and 3564 for the model fit with a frozen and thawed absorption/abundance parameter respectively; ^g Center - an additional power law model component for this region, with the best fit parameters $\Gamma = -3.47_{-0.07}^{+1.79}$ and $\Gamma = -0.29_{-3.21}^{+0.18}$ for fixed and thaw absorption respectively.

TABLE 6
PHYSICAL PARAMETERS OF THE REGIONS^a

Region	Norm ^b [10 ⁻⁶ photons cm ⁻² s ⁻¹]	Area ^c [arcsec ²]	n_e^d [cm ⁻³]	P_{th}^e [10 ⁻¹⁰ dyne cm ⁻²]
NLobe	10.84±2.19	20.82	0.18±0.02	2.60±0.39
NLobe1	0.552±0.145	23.93	0.038±0.005	2.31±1.25
NHspot	7.28±1.17	8.08	0.24±0.02	4.11±0.56
SHspot	4.58±0.31	9.55	0.17±0.01	12.20±1.5
SJet	0.91±0.18	30.69	0.043±0.004	2.90±1.27
SLobe	2.82±0.78	251.13	0.026±0.004	0.68±0.19
SLobe1	0.74±0.18	91.02	0.022±0.003	1.62±1.03
Center	19.9±13.9	75.93	0.128±0.045	2.17±0.93
Total	51.38±4.16	1751.77	0.043±0.002	0.81±0.05
EArm	4.74±2.01	58.73	0.071±0.015	0.91±0.26
HBranch	10.63±2.84	192.99	0.059±0.008	0.75±0.14
HBranchS	8.19±1.66	115.44	0.07±0.01	1.07±0.17
Core	4.2±0.5	4.91	0.23±0.01	50.41±18.77
Core_ext	3.98±0.47	57.45	0.066±0.004	17.29±10.59

^a Density and thermal pressure in the selected regions calculated using the results of a thermal model fit to the spectra.

^b Normalization of thermal bremsstrahlung model in units of 10⁻⁶ photons cm⁻² s⁻¹. Norm = $\frac{3.02 \times 10^{-15}}{4\pi D^2} \int n_e n_I dV$, where n_e is the electron density (cm⁻³), n_I is the ion density (cm⁻³), and D is the distance to the source (cm);

^c Area in units of arcsec². The third dimension assumed in calculation of the electron density was set to 1 kpc.

^d Electron density in cm⁻³. 1 σ errors due to the uncertainty on normalization.

^e Thermal pressure in units of 10⁻¹⁰ dyne cm⁻². 1 σ errors due to the normalization and temperature errors only.

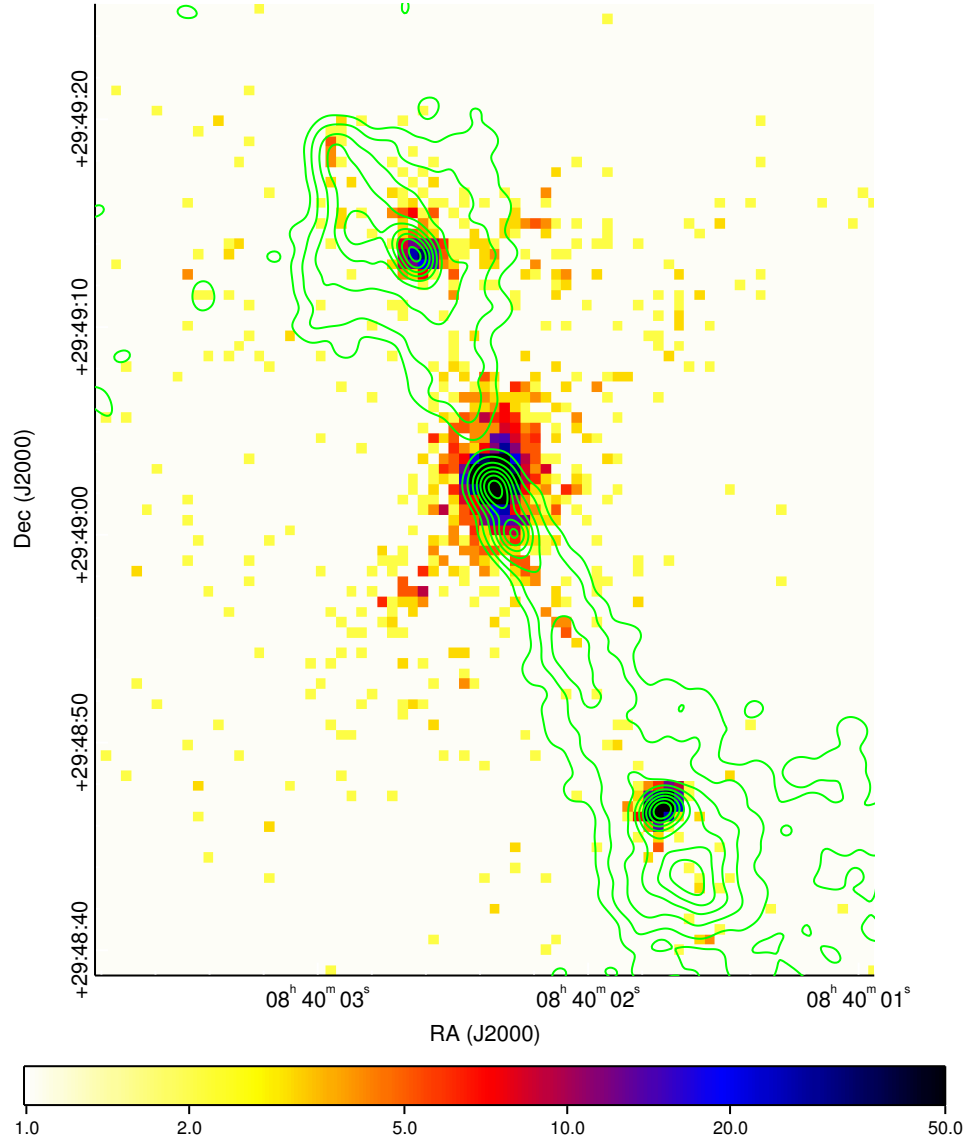


FIG. 1.— *Chandra* ACIS-S image of the 4C+29.30 radio galaxy in the 0.5 – 7 keV energy band. The four individual observations have been merged into one image which was binned to show the scale of ACIS-S pixels, 1 pixel = 0.492". The image is overlaid with the contours from VLA 1.45 GHz map of van Breugel et al. (1986) obtained from the NRAO archives and processed by Cheung (2004). The contours are the fractions of the highest contour (0.04, 0.042, 0.044, 0.12, 0.24, 0.48) \times 0.005 Jy/beam with a clean beam size of $1'' \times 1''$. The color bar indicates a number of counts per pixel.

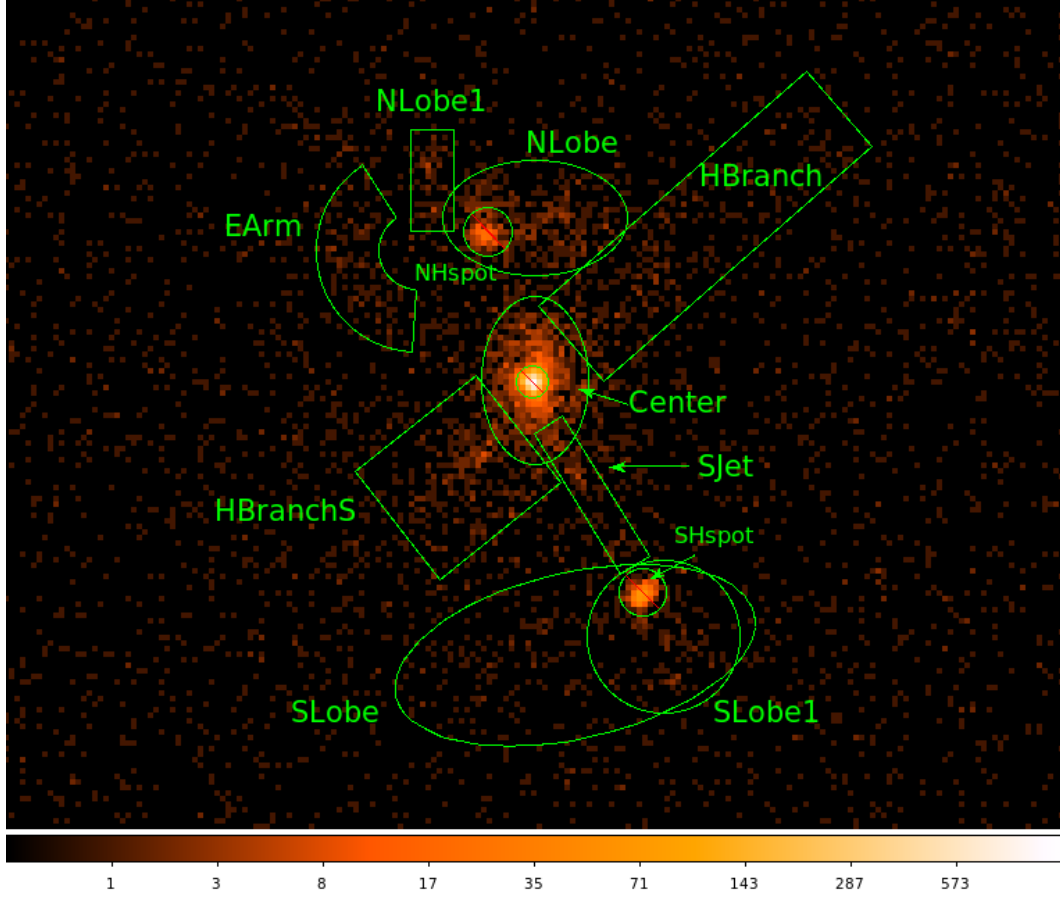


FIG. 2.— *Chandra* ACIS-S image of the 4C+29.30 radio galaxy in the 0.5 – 7 keV energy range. Components of the emission are marked by names and regions. The same regions were used for spectral extractions. (Note that some regions were excluded in extraction of the diffuse emission and they have been marked by red lines.) The pixel size is equal to $0.492''$, i.e., the ACIS pixel size.

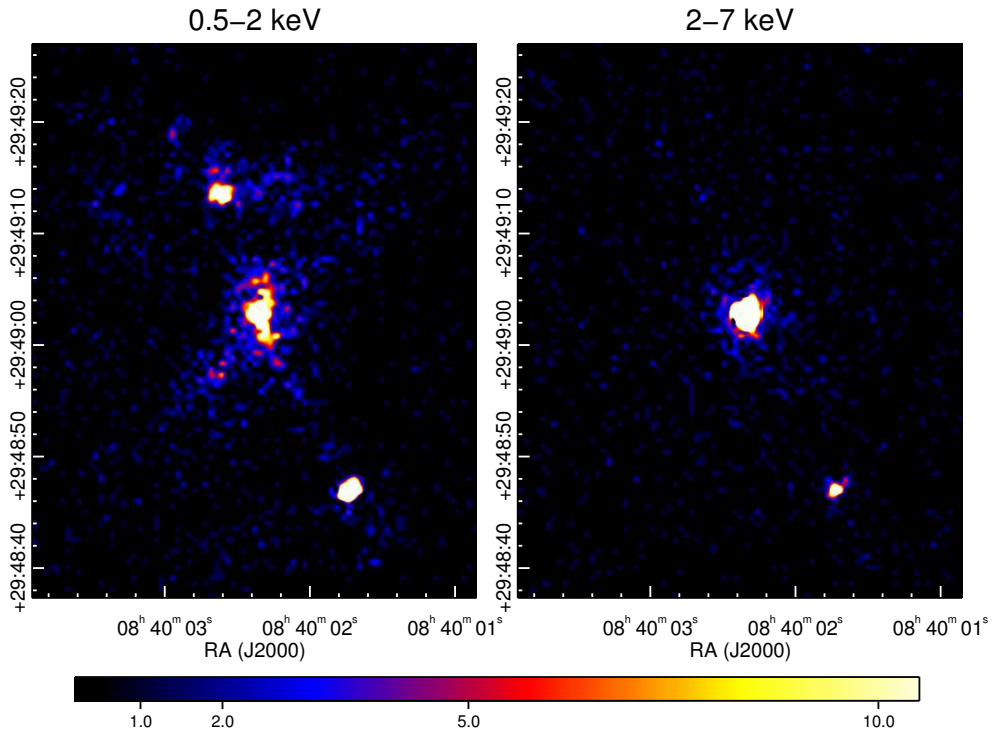


FIG. 3.— *Chandra* ACIS-S images of the 4C+29.30 radio galaxy in the soft (0.5 – 2 keV; left) and hard (2 – 7 keV; right) band. The images were smoothed with the Gaussian kernel with $\sigma = 0.75''$. The color scale indicates number of counts as marked in the color bar. The images are on the same physical scale. The core and the southern hotspot are prominent in the hard band image.

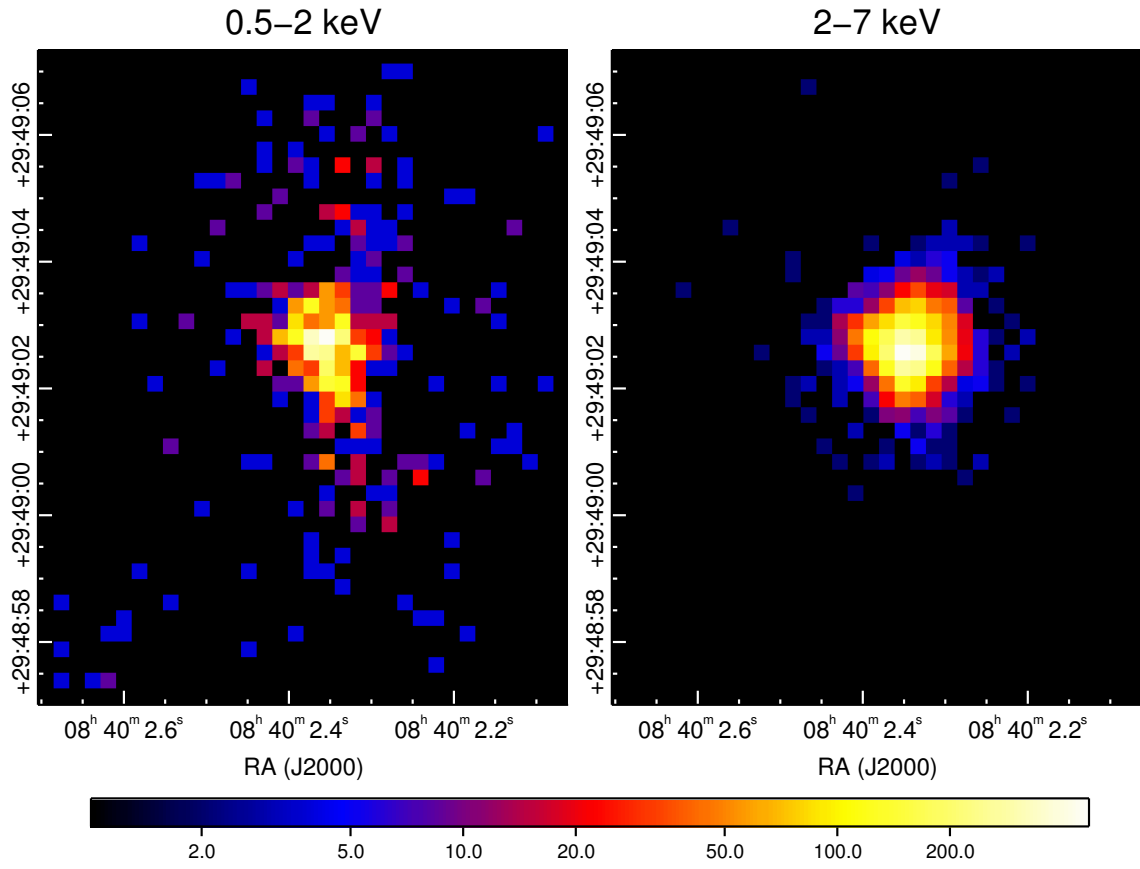


FIG. 4.— ACIS-S images of the core regions in two bands, soft 0.5 – 2 keV and hard 2 – 7 keV. The pixel size is 0.242 arcsec (0.5 of the original ACIS-S pixel size). The color scale indicates a number of counts in the image pixel.

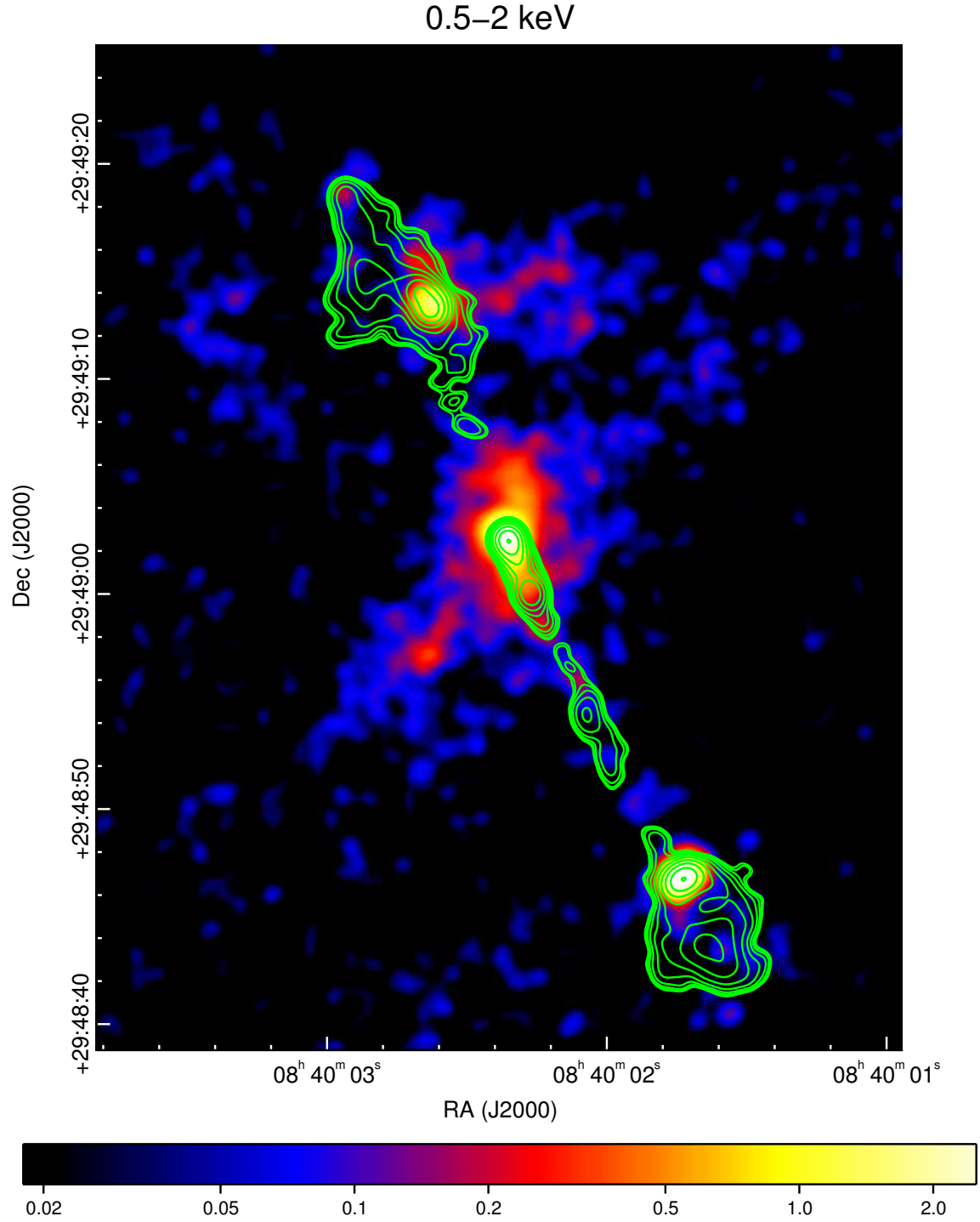


FIG. 5.— Smoothed *Chandra* ACIS-S image overlaid with contours from VLA map at 5 GHz. Only X-ray photons from 0.5–2 keV range were included in the image. The original image was binned by a 1/4 of the original ACIS-S pixel size and then smoothed with the Gaussian function ($\sigma = 0.5''$). The utilized radio map was initially presented in Sambruna et al. (2004) using archival data originally published by van Breugel et al. (1986). The scale is indicated in the bottom color bar.

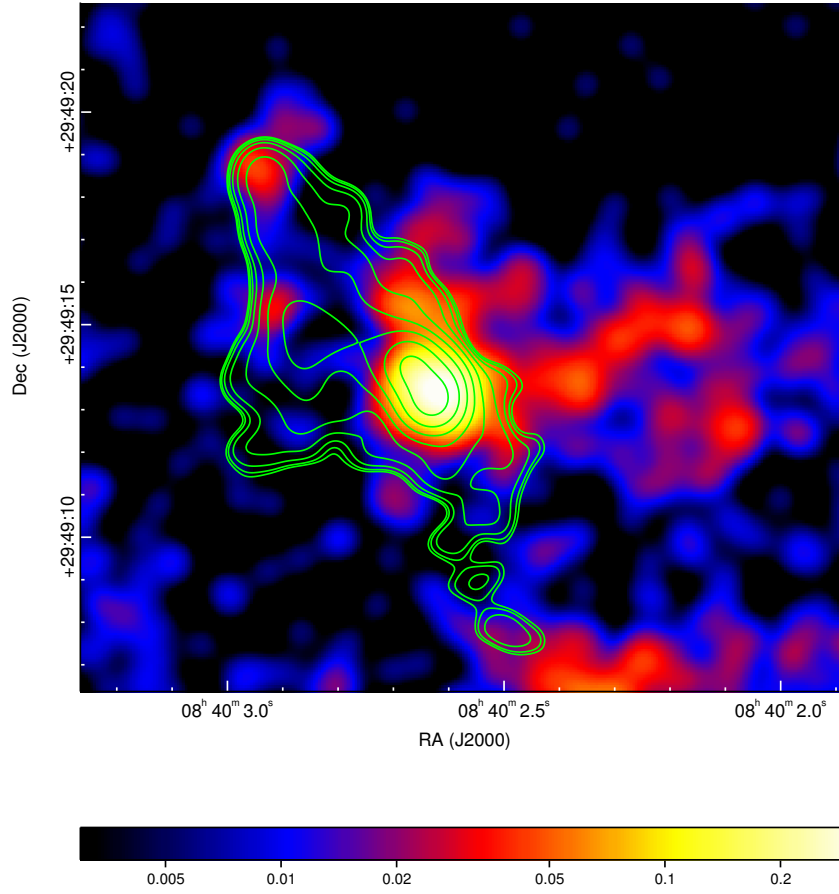


FIG. 6.— ACIS-S image of the northern lobe and hotspot regions in the energy range 0.5 – 2 keV overlaid with radio contours from the VLA 5 GHz image. The X-ray image was binned to 0.125'' pixel size and smoothed with the Gaussian with $\sigma = 0.5''$.

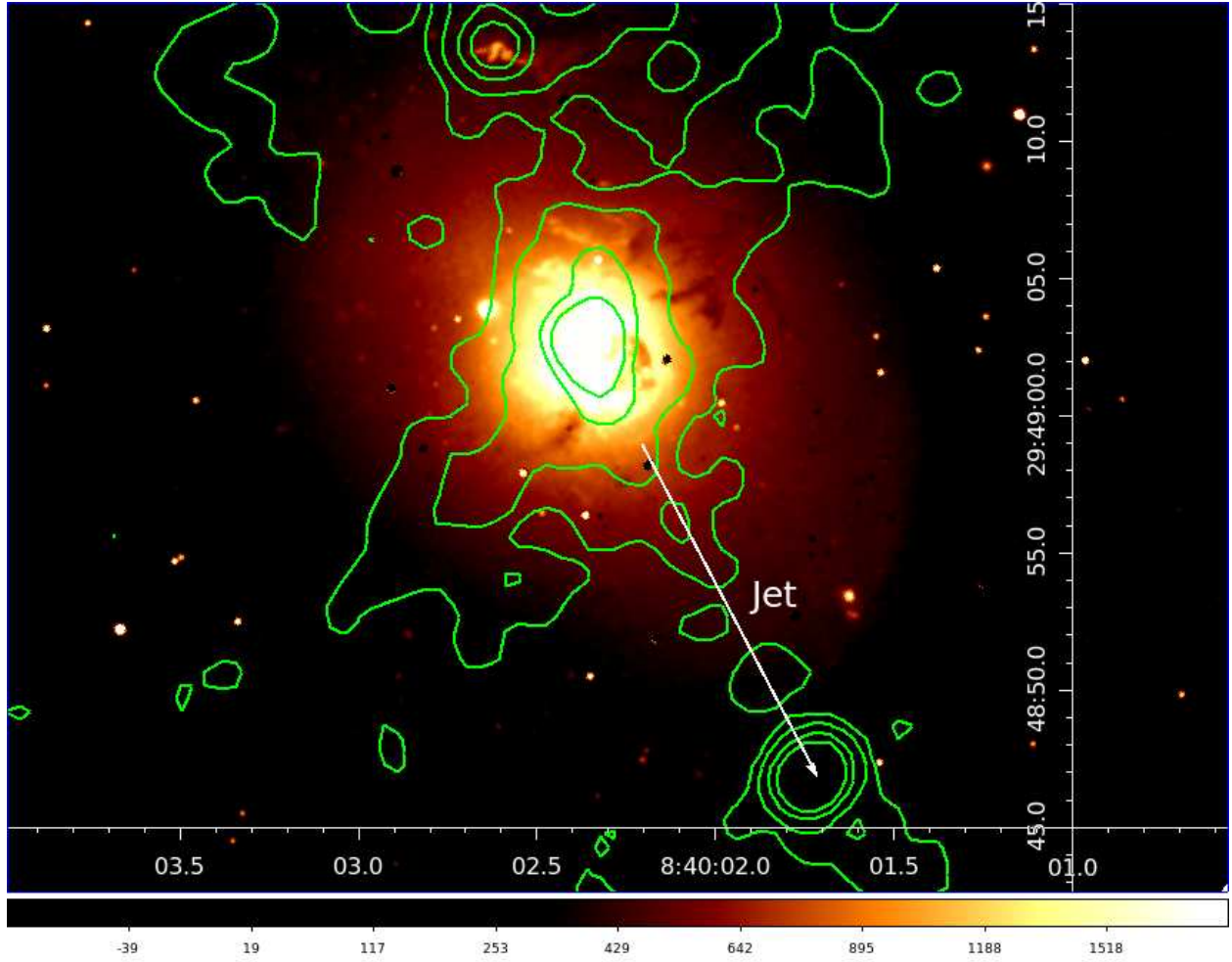


FIG. 7.— Optical image of the host galaxy obtained from the HST archives (HST-STIS CCD, the wavelength peaks at 5840\AA). The colors represent intensity. The Chandra X-ray contours are overlayed on the image. The SW direction of the radio jet is marked by a white arrow. Dark filaments of dust start in the central regions and extend perpendicular to the jet axis.

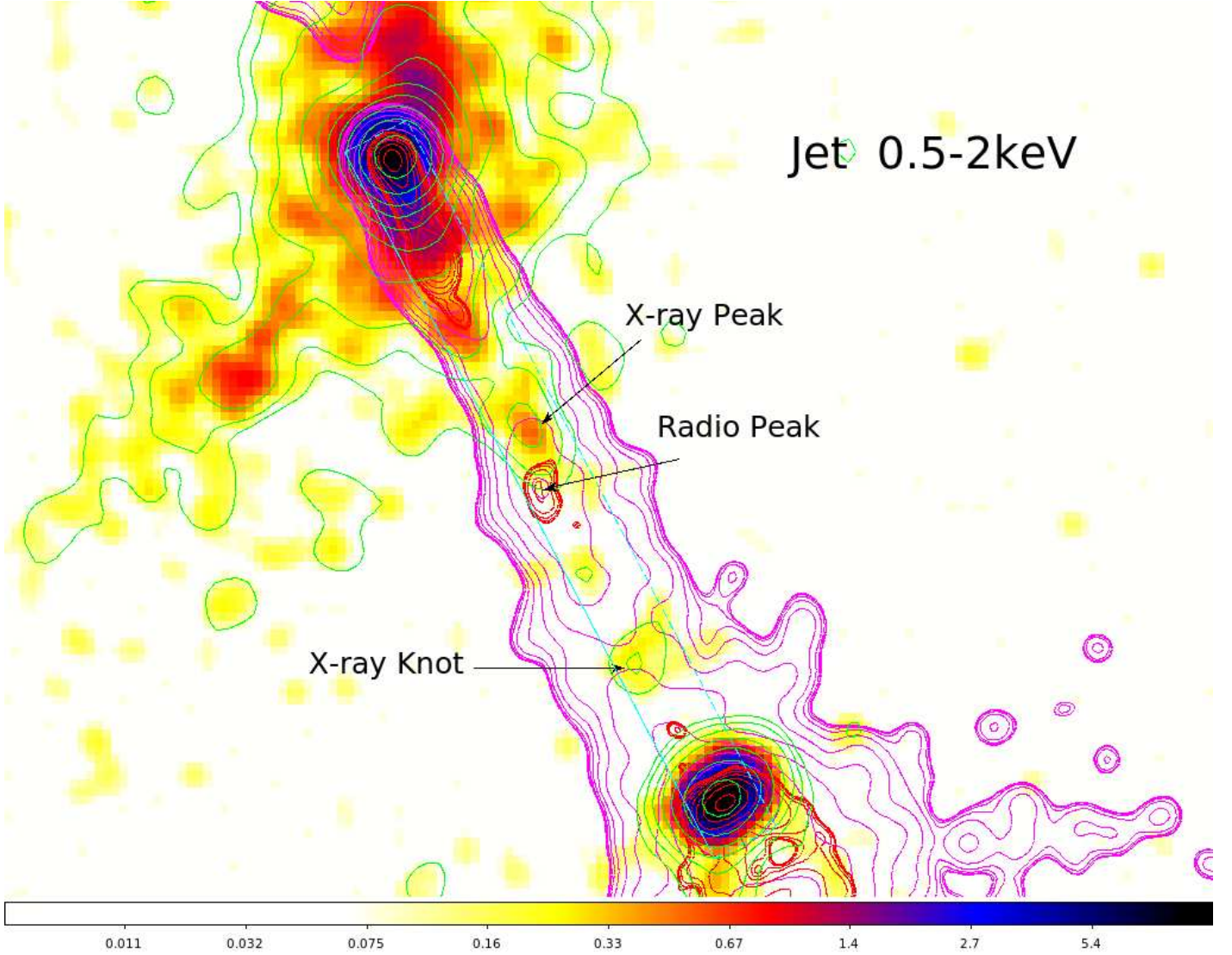


FIG. 8.— X-ray image ($0.5 - 2$ keV) of the 4C+29.30 southern region where the radio jet is observed. Green contours mark X-ray emission, magenta contours show 1.4 GHz emission and red contours mark 5 GHz emission based on $1''$ and $0.5''$ resolution maps, respectively. Cyan marks the box regions assumed for the extraction of the jet spectrum. We mark the positions of X-ray and radio peaks in the map corresponding to the features in the profiles. Both radio images were reprocessed by Cheung (2004) from archival VLA data published by van Breugel et al. (1986).

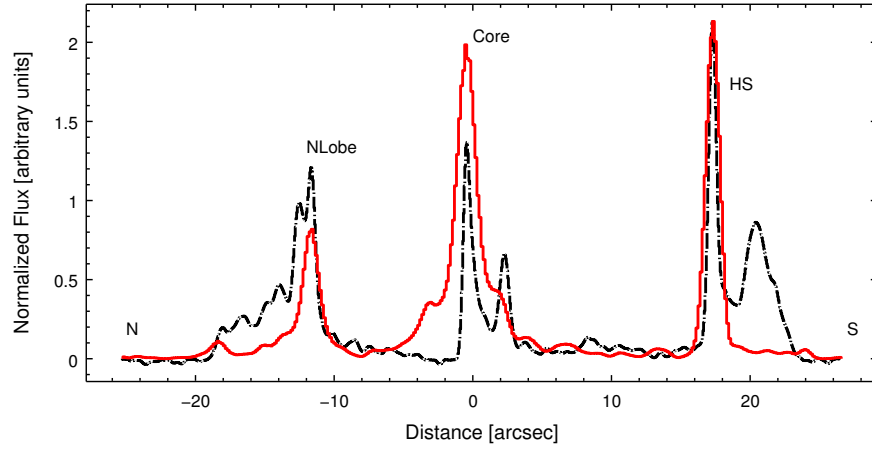


FIG. 9.— X-ray (0.5-2 keV) and radio (5 GHz) profiles extracted from a $4''$ wide box aligned with the jet at P.A.= 24° (north is to the left and south to the right). The radio 5 GHz profile is plotted with a dashed line and the X-ray profile is plotted as solid (red) line. The profiles are aligned at the core and normalized to the brightest peak to best compare the morphology in two bands.

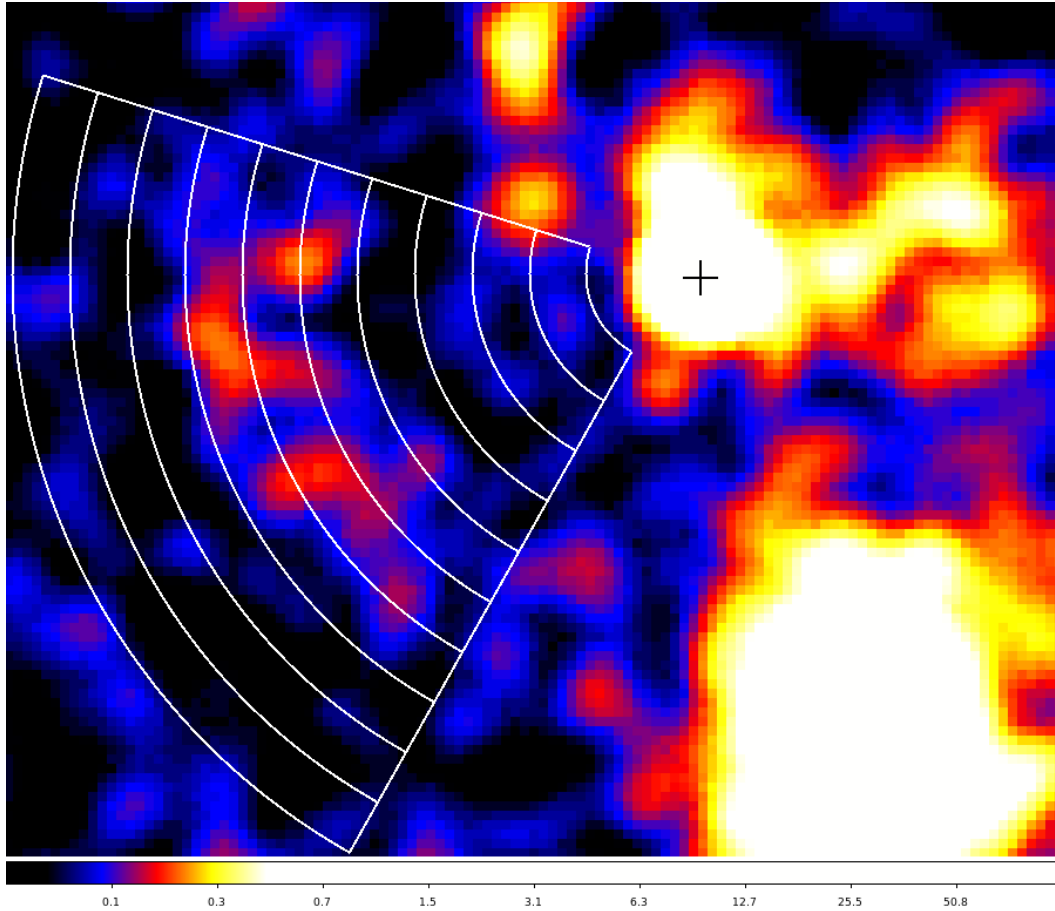


FIG. 10.— X-ray emission in the vicinity of NHSpot and EArm overlaid with regions (white) used to construct the surface brightness profile in Figure 11. Black cross marks the peak position of NHspot and the initial reference point for the regions.

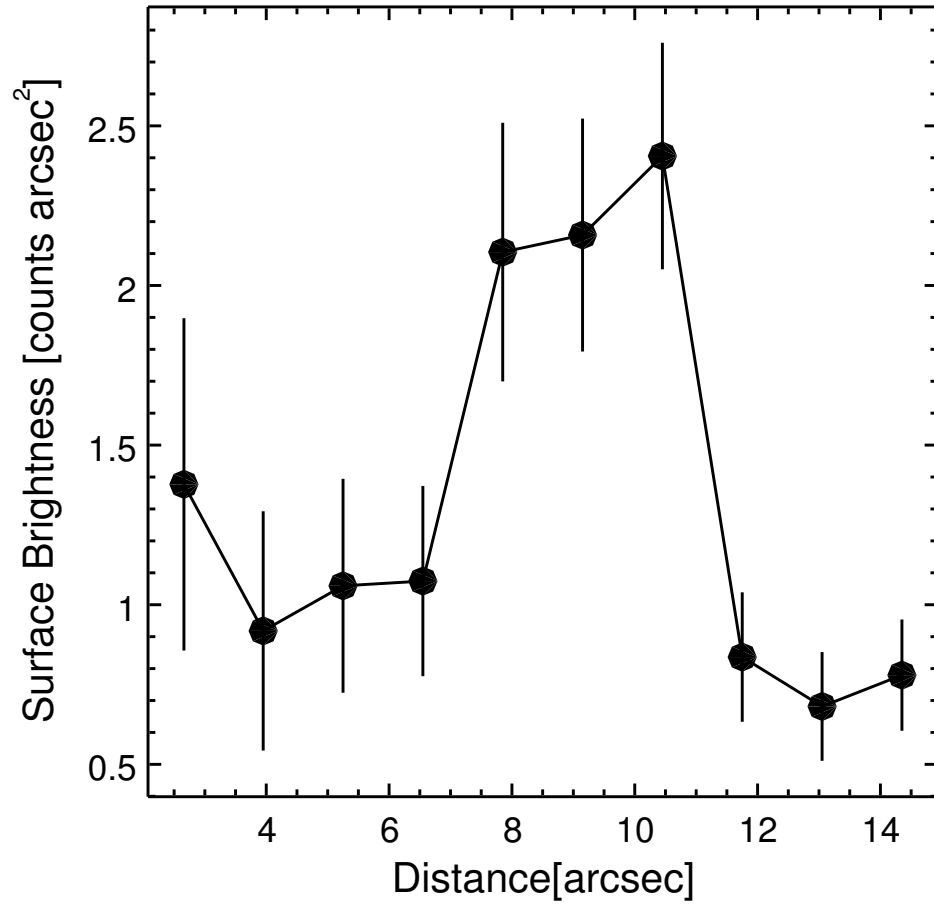


FIG. 11.— X-ray surface brightness profile (in units of counts arcsec⁻²) across EArm constructed using the regions marked in Figure 10. The distance is measured from the NHspot peak brightness marked in the region figure with black cross.